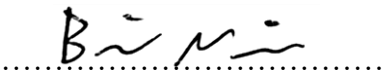## uS

University of Stavanger

Faculty of Science and Technology

MASTER'S THESIS

Study program/ Specialization: Marine- and Offshore Technology	Spring semester, 2019 Open / ~~Restricted access~~
Writer: Bjørnar Nitter	*B̃ M̃* ………………………………… (Writer's signature)

Programme coordinator:

  Prof. Muk Chen Ong

Supervisors:

  Prof. Muk Chen Ong

    Dr. Guang Yin

Thesis title:

  CFD investigation of flow through an orifice inside a pipe

Credits (ECTS): 30

Key words: Computational Fluid Dynamics, CFD, OpenFOAM, Orifice, Obstruction flowmeter, Discharge coefficient, Laminar flow, Turbulent flow, Pipe	Pages: 61 + enclosure: 11 Stavanger, June 14, 2019 Date/year

Abstract

Flow measurement is found in a large variety of industries and for different types of fluids. Orifice flow meters are widely used for measuring the flow rate in pipelines due to its small size in the piping system and ability to output the flow rate with satisfying accuracy. The main problems with the orifice flow meter are the unrecoverable pressure loss and due to the shear forces exerted from the orifice walls onto the flow, inaccurate flow rate measurement as well as the vortex shedding behind the orifice.

Numerical studies have been performed using the open source CFD code OpenFOAM to investigate the flow through a circular square edged orifice with various thicknesses and diameters inside a pipe. The orifice thickness to pipe diameter ratio (t) varies between $0.125 \leq t \leq 2$ and the orifice diameter to pipe diameter (β) varies between $0.25 \leq \beta \leq 0.75$. The discharge coefficients for the different orifice characteristics at different Reynolds numbers have been determined. Simulations are performed in two different regimes, a laminar flow regime at $0 \leq Re \leq 400$ and a turbulent flow regime at $2\,500 \leq Re \leq 40\,000$. The effects of different Re, β and t on the flow characteristics are discussed by presenting the streamwise velocity contours, streamlines and Q-criterion contours.

The results of the present study have been compared with the previous published numerical and experimental results as the validation study. The discharge coefficients are in satisfying agreement with the previous published numerical and experimental data.

Acknowledgement

Contents

Figures

Tables

Symbols

A_0	Orifice cross sectional are
C_d	Discharge coefficient
Co	Courant number
D	Pipe diameter
d	Orifice diameter
g	Gravitational acceleration
k	Turbulent kinetic energy
L	Pipe length
L_h	Hydraulic length
L	Axial pressure
Q	Q-criterion
$\dot{Q}$	Flow rate
r	Pipe radius
Re	Reynolds number
t	Orifice thickness
U	Flow velocity
V_{avg}	Average fluid velocity
$\bar{u}$	Average flow velocity
u'	Fluctuating velocity component
u^+	Ratio of velocity to the shear velocity
u^*	Friction velocity
u_{max}	Maximum horizontal velocity
y	Vertical distance normal to the wall
y^+	Non-dimensional vertical distance
β	Orifice diameter to pipe diameter ratio
$\delta_{Sublayer}$	Thickness of viscous sublayer
ε	Specific dissipation rate

ρ	Fluid density
τ	Shear stress
τ_w	Wall shear stress
Δt	Numeric time-step interval
μ	Dynamic viscosity
μ_t	Turbulent viscosity
ν	Kinematic viscosity
ω	Specific dissipation rate

Abbreviations

2D	Two-dimensional
3D	Three-dimensional
CFD	Computational Fluid Dynamics
RANS	Reynolds-Averaged Navier-Stokes
SOU	Second-Order Upwind
SST	Shear Stress Transport

Chapter 1 Introduction

This study investigates the three-dimensional (3D) flow through an orifice inside a pipe for both laminar and turbulent flow. The chosen geometry for the orifice is a square edged circular geometry inserted at $L/2$ of the pipe (where L is the total length of the pipe).

The main objective of this study is to validate the present results with previous numerical and experimental results. This is done by studying the pressure drop of the flow through the orifice and presenting the discharge coefficient for each orifice characteristics for different Re.

Secondly, the present validated CFD model is used to present results on orifice characteristics which previously has not been extensively researched. The orifice characteristics investigated in this study is the thickness of the orifice to pipe diameter ratio t in the range $0.125 \leq t \leq 2$ and orifice diameter to pipe diameter β in the range $0.25 \leq \beta \leq 0.75$. The Reynolds number investigated are in the range $4 \leq Re \leq 400$ for laminar flow and $2\,500 \leq Re \leq 40\,000$ for transitional and turbulent flow.

The present study can contribute to a better understanding of the flow characteristics of laminar and turbulent flow through an orifice inside a pipe, and contribute to improved selection of appropriate orifice flowmeters.

The present study is based on the open source code OpenFOAM, version 2.4.0, with the use of computational resources from NTNU, Vilje.

1.1 Background and motivation

Flow measurement is widely found in engineering applications and for different fluids. A large variety of different flow meters has been created throughout the years. One of the first ever use of flowmeters that have been recorded dates back to around 5000 B.C. in Mesopotamia. The water flow measurement was used to control the flow of the water supplied into the cities. An obstruction was placed in the water channel to monitor the height of the water flow flowing over the obstruction. In 1450, the first flow measurement to measure the wind speed was invented by the Italian architect Battista Alberti. The mechanical anemometer consisted of a disk rotating perpendicular to the wind. Due to the force from the wind, the tilting of the disk could indicate the wind speed (Cottrell, 2006). In modern processing facilities, the flow rate in

the processing pipes needs to be measured accurately to achieve an optimal economic operation. There are several ways to measure the flow rate in processing systems. The flow measurement techniques for processing facilities can be divided into four main types (Cottrell, 2006):

Velocity flow meters measures the fluid velocity at the center of a fixed pipe. This can be done by measuring the static axial pressure in the flow at different locations in the pipe and applying the pressure difference into Bernoulli's equation to determine the velocity of the fluid. These types of flow meters are not suitable for the pipes with small diameter, where the boundary layer on the wall has a significant effect on the flow.

Positive displacement meters measure the volume of the fluid by temporarily trapping the fluid in pockets with housed rotating components. The flow causes the components to rotate, and the flow rate is directly proportionate with the rotational speed of the rotors. Flowmeters in this category are not suitable for the pipes with large diameters and for high-speed flows.

Electromagnetic meters use Faraday's law of electromagnetic induction to determine the fluid flow rate. The flow passes a magnetic field and the flow rate is proportionate with the potential difference in the flow passing the magnetic field. These flow meters are accurate for measuring corrosive liquids. However, they will only work if the fluid in the flow is conductive and the pipe is non-conductive.

Obstruction meters measure the flow in a pipe by inserting an obstruction plate inside the pipe and measuring the pressure of the flow on each side of the obstruction plate. The flow in the pipe is contracted by the change of the cross-section area created by the obstruction plates. The flow is then accelerated because of the mass conservation, which causes a pressure drop due to the energy conservation. The pressure difference measured by the pressure tapping in the upstream and downstream of the flow is combined with Bernoulli's equation to obtain the flow rate.

Several shapes of the obstruction are presented throughout the years with different application benefits. The most common obstruction shapes are as follows:

Nozzle: A gradual constriction of the flow is achieved by an elliptical contour approach section in the shape of a nozzle. This shape creates an intermediate pressure drop, which is appropriate for measuring flow rates in slurry systems.
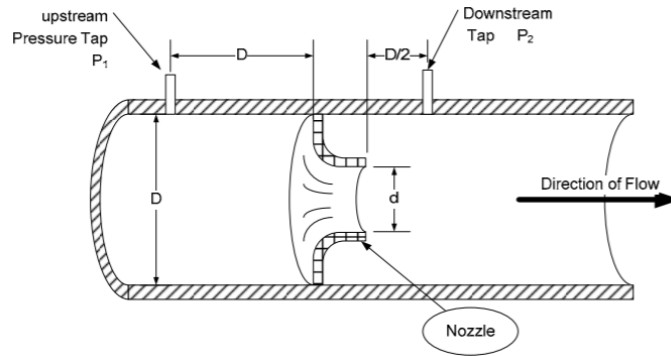
Figure 1.1 Nozzle flowmeter (Cottrell, 2006, p. 8)

Venturi: A gradual contraction and extraction of the flow in the downstream and upstream is accomplished by a long nozzle shaped inlet and outlet of the obstruction plate. This shape creates a lower pressure drop and drag force than that of the nozzle shape.
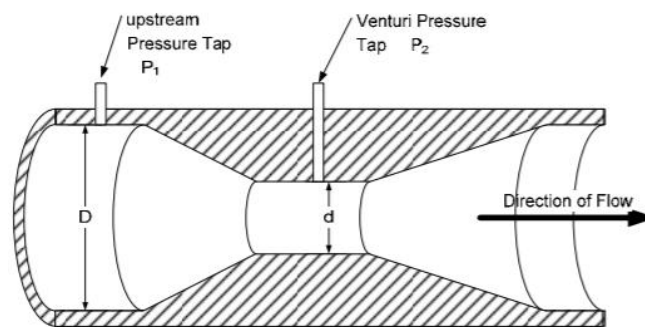
Figure 1.2 Venturi flowmeter (Cottrell, 2006, p. 7)

Orifice: A sudden constriction of the flow is achieved by a flat plate with a circular hole in the middle. This shape causes a high pressure drop and the largest drag force out of the three shapes.
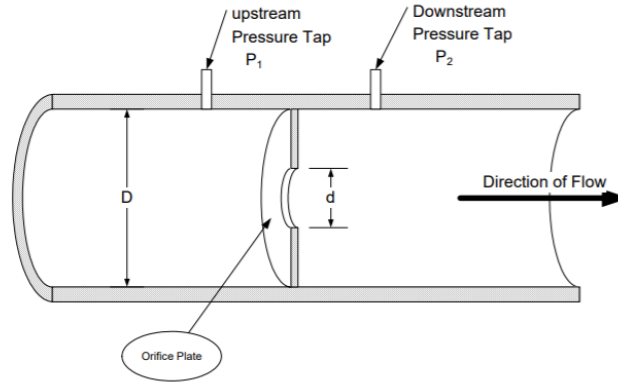
Figure 1.3 Orifice flowmeter (Cottrell, 2006, p. 3)

The most common used obstruction flow rate meter is the orifice flowmeter, due to its simplicity and the small volume it occupies in the piping system compared with other obstruction flowmeters. Based on this engineering background, flow through the orifice flowmeter shape is investigated in this study. The theoretical background behind the orifice flowmeter is covered in Section 2.7.

1.2 Previous work

Flow through an orifice has been extensively studied both by experiments and numerical simulations. This section will cover a portion of the important experimental and numerical studies conducted on the topic of flow through an orifice flowmeter.

Experimental studies: A large number of experimental studies have been previously carried out to investigate the flow characteristics inside an orifice flowmeter. One of the first studies done on orifice flowmeters was carried out by Johansen (1930). He investigated the flow characteristics from laminar to turbulent at $0 \leq Re \leq 25\ 000$ ($Re = UD/\nu$, where U is the mean flow velocity, D is the pipe diameter and ν is the kinematic viscosity of the fluid), with the orifice diameter to the pipe diameter ratio range of $0.209 \leq \beta \leq 0.794$ ($\beta = d/D$) in two series of experiments: Firstly, a visual observation of water through the different orifices in a glass pipe is conducted by injecting colored matters into the stream. Secondly, determination of discharge coefficients for the orifices is made by mounting the orifices in a straight smooth brass pipe and monitoring the pressure difference of water with low velocities and highly viscous oils. Johansen (1930) observed that the upper limit of Re for the steady flow through

the different orifices was approximately $Re = UD/\nu = 10$. He also discovered that the discharge coefficients rise steeply at Re ranging from 0-160 for $\beta < 0.6$ and from 0-1000 for $\beta = 0.794$ before descending to a final value. Sahin & Ceyhan (1996) investigated the effects of the orifice plate thickness and Reynolds number by carrying out experiments and numerical simulations. The experimental setup consisted of a hydraulic circuit with the pipe diameter of 13.7mm, a gear pump and a by-pass valve for regulating the flow rate. The pipe length was set to be $170D$, the orifice diameter β to be $D/2$ and with the orifice thickness range of $1/16 \leq t \leq 1$. The Reynolds numbers range under investigation was $0 < Re \leq 150$. The pressure distribution was monitored by an inclined multitube manometer. Sahin & Ceyhan (1996) observed that altering the thickness of the orifice did not change the separation of the flow through the orifice significantly. The discharge coefficients for $t = 1/16$ was in good agreement with the previous published experimental data by Johansen (1930). Gao & Wu (2019) investigated the difference in the transitional flow characteristics of mineral oil through a single and a two staged orifice using experimental studies. The characteristics of the flow was monitored by flow- and pressure sensors. Gao & Wu (2019) found that the discharge coefficients obtained from the two-stage orifice are higher than those obtained from a single orifice with the same diameter, which was consistent with the theoretical calculations. Further discussion and comparisons with numerical models are covered in next paragraph.

Numerical studies: Dickerson & Rice (1969) investigated flow through orifices with t of 1~4 at Re ranging from 27~7000. Dickerson & Rice (1969) followed the Langhaar entrance flow solution with $\beta < 0.1$ and obtained a good agreement with the experimental results for the discharge coefficient (Miller & Nemecek 1958). Lakshmana & Sridharan (1971) presented a theoretical solution for determining the discharge coefficient based on Hornbeck's flow entrance model (Hornbeck 1964), which is used to predict the discharge coefficient for laminar flow in long orifices with small β. Lakshmana & Sridharan (1971) compared the theoretical solution with the experimental data and found that the solution is valid with $t > 2$ and at an orifice Reynolds number of $Re < 300$. Sahin & Ceyhan (1996) also carried out numerical simulations. The numerical solutions based on the steady Navier-Stokes equations was obtained by finite difference method at $0 \leq Re \leq 150$ with $1/16 \leq t \leq 1$ and constant β=0.5. Sahin & Ceyhan (1996) obtained a good match between the numerical and experimental results. The streamlines and vorticity contours showed that there are two eddies in the upstream and downstream of orifice plate. Hollingshead et al. (2011) carried out numerical simulations to obtain the discharge coefficient in four different orifice flowmeters: standard concentric-,

venturi-, V-cone- and wedge orifice based on laminar flow conditions at $Re < 2300$ and turbulent flow conditions at $Re \geq 2300$ using Reynolds Average Navier-Stokes (RANS) equations combined with the $k - \varepsilon$ model. Hollingshead et al. (2011) discovered that at low Re, the discharge coefficient decreased rapidly with decreasing Re for Venturi, V-cone and wedge flowmeters. The standard concentric orifice plate meter did not follow the general trends of the other flow meters. Instead, as Re decreased, the discharge coefficient increases to a maximum value before aggressively drops off with further decreasing Re. Gao & Wu (2019) investigated the difference in the transitional flow characteristics of mineral oil through a single and a two staged orifice using numerical studies. The numerical study was conducted by solving the steady RANS equations combined with the $k - \varepsilon$ turbulence model. They discovered that the discharge coefficient of the two staged orifices was greater than that of the single staged orifice with the same diameter as the secondary orifice. They also discovered that under the same flow rate, the pressure drop of the two staged orifices was less than that of the single staged orifice. It was concluded that the two staged orifices can improve the stability of the flow field at the outlet of the orifice. Laminar and turbulent flow through a square edged orifice plate was investigated by Tunay et al (2004) using numerical simulations. The $k - \varepsilon$ model was used to study the effects of the Reynolds number and orifice thickness on the characteristics of the flow through the orifice plate, at $0 \leq Re \leq 2 \cdot 10^5$ with $1/12 \leq t \leq 1$ and β=0.6. One of the findings in this study was that C_d values are more sensitive to the change of Re with small t than large t. Using larger t caused less pressure drop and variation in C_d for both laminar and turbulent flow. Separation and re-attachment of the flow occurred in the bore of the orifice plates with the thickness of $1/4 \leq t \leq 1$. Ding & Wang (2015) studied the energy dissipation in three different orifice plates with different edges at $Re = 1.8 \times 10^5$. The $k - \varepsilon$ model was used to determine the energy loss, wall pressure and the backflow length for sharp-edged-, square-edged- and round-edged orifice plates. They discovered that the sharp-edged orifice plate causes the highest energy dissipation, the square edged causes the lowest energy dissipation and vice versa for the resistance cavitation damage of the orifice plates. Effect of different β and turbulence models on turbulent flow through the orifices was investigated by Eiamsa-ard et al (2008). The Reynolds stress model (RSM) was compared with the $k - \varepsilon$ model with different numerical schemes and validated against the experimental data at $Re = 1.84 \times 10^4$ for $\beta = 0.5, 0.6$ and 0.8. They found that both turbulence models were in good agreement with the experimental data, but Reynolds stress model was found to give better performance than the $k - \varepsilon$ model. Best results with the $k - \varepsilon$ model was found to be in

combination with the Second Order Upwind (SOU) scheme. They observed from velocity contours that the size of the recirculation at the outlet of the orifice plate increased with decreasing β.

1.3 Summary

The literature review presents a number of previous experimental and numerical studies carried out on the topic of orifice flowmeters. The majority of these studies was based on investigating the effect of the orifice thickness at different Re. In the previous studies, the effects of different β have not been extensively studied. The numerical simulations to determine the discharge coefficients are validated in the above-mentioned literatures, but no comprehensive study is performed to investigate the effects of different orifice characteristics on the flow fields. This gives an opportunity to investigate a variety of different orifice characteristics in both laminar and turbulent regime, and to improve the knowledge on how these characteristics affect the behavior of the flow through the orifice.

1.4 Outline of thesis

The structure of the thesis is organized in the following way:

Chapter 2 presents the theory of viscous flow inside a pipe. This includes the theory of laminar and turbulent flow, the basic knowledge of the orifice flowmeter and the discharge coefficient.

Chapter 3 provides an introduction to Computational Fluid Dynamics (CFD), the Finite Volume Method and the software used. The governing equations and the k-ω SST turbulence model used in this study are also explained.

Chapter 4 presents the numerical setup, results and discussion of laminar flow through a square edged orifice inside a pipe.

Chapter 5 presents the numerical setup, results and discussion of turbulent flow through a square edged orifice inside a pipe.

Chapter 6 gives a conclusion and recommendations for further work.

Chapter 2 Flow inside a pipe

The present chapter explains the theoretical background of viscous flow inside a pipe and the orifice flowmeter.

2.1 Concept of laminar and turbulent flows

The difference between laminar and turbulent flow was demonstrated by Osborne Reynolds in 1883, by injecting a small stream of dye into a tube with water flowing and observing the behavior of the dye (Kundu & Cohen, 2008, p.309). Reynolds observed that the dye stream was following a behaved straight line at lower flow rates, the flow was moving in parallel layers and did not mix and it was called laminar flow. Increasing the flow rate caused the dye stream to break up and irregular motion of the dye occurred. Macroscopic mixing perpendicular to the flow direction was observed, and this type of flow was called turbulent flow. Fig. 2.1 shows behavior of laminar and turbulent flow inside a tube.
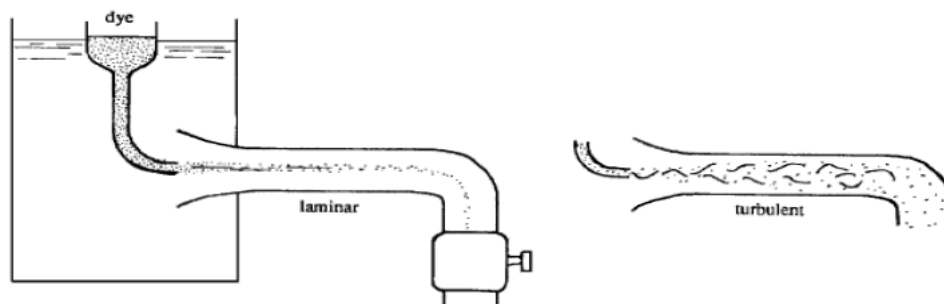
Figure 2.1 Behavior of dye injected into laminar and turbulent flow (Kundu & Cohen, 2008, p. 296)

2.2 Reynolds number

In principle, the flow can be characterized by the ratio of inertia force to viscous force. This ratio is known as the Reynolds number (Çengel & Cimbala, 2017) and is expressed as shown in Eq. (2.1).

$$Re = \frac{Inertial\ forces}{Viscous\ forces} = \frac{V_{avg}D}{\nu} = \frac{\rho V_{avg}D}{\mu} \tag{2.1}$$

where V_{avg} is the free stream velocity, D is the characteristic length of the geometry, $\nu = \frac{\mu}{\rho}$ is the kinematic viscosity. Under typical empirical conditions, the flow in a circular pipe is laminar for $Re \leq 2300$, transitional for $2300 \leq Re \leq 4000$ and turbulent for $Re \geq 4000$ (Çengel & Cimbala, 2017).

2.3 Entrance region

At the inlet of the pipe, the frictional forces exerted from the wall onto the flow are negligible and the velocity of the flow is constant in the radial direction, this region is called the irrotational core flow region. As the flow continues into the pipe, the viscous shearing forces of the flow is starting to affect the flow velocity distribution and the flow is divided into two regions: an irrotational region where friction forces are negligible and velocity remains constant, and a region where the viscous forces are significant and the velocity of the flow is reduced. These two regions combined is called the velocity boundary layer. The region beyond the entrance region is called the hydrodynamic fully developed region, and is achieved when the velocity profile is fully developed and remains unchanged. Fig. 2.2 shows an illustration of the flow development in a pipe.
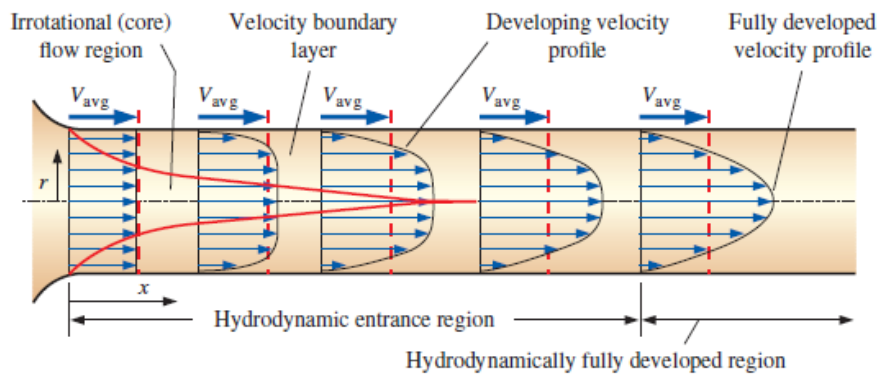
Figure 2.2 Entrance region diagram (Çengel & Cimbala, 2017, p. 355)

The velocity profiles of laminar and turbulent are different. In the laminar flow regime, the fully developed velocity profile is parabolic, while the turbulent velocity profile is observed to be

flatter or "fuller" due to the eddy motion and intensive mixing in radial direction. The difference in velocity profiles between laminar and turbulent flow are shown in Fig. 2.3.
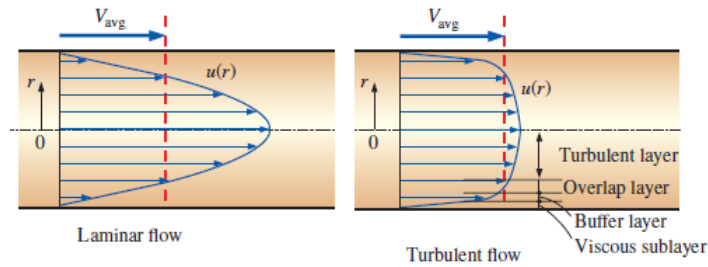
Figure 2.3 Fully developed velocity profile (Çengel & Cimbala, 2017, p. 368)

According to Çengel & Cimbala (2017), the hydrodynamic length is the distance from the pipe inlet to the region where wall shear stress (τ_w) (or the friction factor) grows to about 2 percent of the fully developed value. For laminar flow, the entry length can be approximated from Eq. (2.2):

$$\frac{L_{h,laminar}}{D} \cong 0.05Re \tag{2.2}$$

In turbulent flow, the entry length is shorter than in the laminar flow. The Reynolds numbers dependency is weaker in turbulent flow. In practical engineering interests, the entrance effect on flow in a pipe after the length of $10\,D$ is not important. The hydrodynamic entry length can be approximated as:

$$\frac{L_{h,turbulent}}{D} \cong 10 \tag{2.3}$$

2.4 Laminar flow

In this section, the flow is assumed to be laminar, steady, incompressible flow and fully developed inside a straight circular pipe. In the fully developed laminar flow, fluid particles move at a constant axial velocity throughout the streamline, thus the velocity profile will be constant in the direction of the flow. Velocity components normal to the pipe is always zero as there is no fluid motion in the radial direction. No acceleration of the flow occurs as the flow is steady.

The velocity profile for laminar flow can be derived from the relationship between viscous forces acting on the pipe walls and the pressure force at the centroid of the surface and the surface area. The following explanation are the theoretical steps to obtain the velocity profile for fully developed laminar flow according to Çengel & Cimbala (2017), terms in Eq. (2.4) are shown in Fig. 2.4.
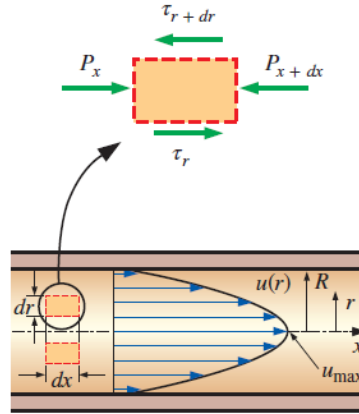
Figure 2.4 Free-body diagram of a ring-shaped differential fluid element with radius r, thickness dr and length dx (Çengel & Cimbala, 2017, p. 357)

The balance of forces on the volume element in the direction of the flow:

$$(2\pi\, r\, dr\, P)_x - (2\pi\, r\, dr\, P)_{x+dx} + (2\pi\, r\, dr\, \tau)_r - (2\pi\, r\, dr\, \tau)_{r+dr} = 0 \qquad (2.4)$$

where r denotes the radius of the volume element and x denotes the streamwise location of the volume element. Rearranging and dividing Eq. (2.4) by $2\pi\, dr\, dx$, obtains:

$$r\frac{P_{x+dx} - P_x}{dx} + \frac{(r\tau)_{r+dr} - (r\tau)_r}{dr} = 0 \qquad (2.5)$$

Taking the limits as $dr, dx \to 0$, Eq. (2.5) becomes:

$$r\frac{dP}{dx} + \frac{d(r\tau)}{dr} = 0 \qquad (2.6)$$

Replacing τ with $-\mu(du/dr)$ and taking μ to be constant gives

$$\frac{\mu}{r}\frac{d}{dr}\left(r\frac{du}{dr}\right) = \frac{dP}{dx} \qquad (2.7)$$

Left side of Eq. (2.7) is a function of r and right side is a function of x. The equality must be held for any values of r and x. To achieve this, dP/dx is set to be constant and integrating Eq. (2.7) with respect to r from $r = 0$ to R can obtain:

$$\pi R^2 P - \pi R^2 (P + dP) - 2\pi R dx \tau_w = 0 \qquad (2.8)$$

Simplifying Eq. (2.8) gives:

$$\frac{dP}{dx} = -\frac{2\tau_w}{R} \qquad (2.9)$$

where τ_w is the shear stress on the surface of the pipe walls as $\tau_w = -\mu \, d\bar{u}/dr$

Therefore dP/dx is constant. Eq. (2.9) is rearranged and integrated with respect to r twice to give:

$$u(r) = \frac{r^2}{4\mu} \left(\frac{dP}{dx}\right) + C_1 \ln r + C_2 \qquad (2.10)$$

Implementing boundary conditions $du/dr = 0$, $r = 0$ (symmetry about the centerline of the pipe) and $u=0$ at $r = R$ (No-slip condition at the walls), the velocity profile $u(r)$ can be obtained:

$$u(r) = -\frac{R^2}{4\mu} \left(\frac{dP}{dx}\right) \left(1 - \frac{r^2}{R^2}\right) \qquad (2.11)$$

It can be determined from Eq. (2.11) that the velocity profile is parabolic with maximum velocity located in the middle of the pipe and zero velocity at the pipe wall.

The averaged velocity for incompressible laminar flow in a circular pipe with radius R is expressed as:

$$V_{avg} = \frac{2}{R^2} \int_0^R u(r) dr = \frac{-2}{R^2} \int_0^R = \frac{R^2}{4\mu} \left(\frac{dP}{dx}\right) \left(1 - \frac{r^2}{R^2}\right) r \, dr = -\frac{R^2}{8\mu} \left(\frac{dP}{dx}\right) \qquad (2.12)$$

Combining Eq. (2.11) and (2.12), the velocity profile can be written as:

$$u(r) = 2V_{avg} \left(1 - \frac{r^2}{R^2}\right) \qquad (2.13)$$

Substituting $r = 0$, it gives $u(r) = 2V_{avg}$ and it can be determined that the averaged velocity in a fully developed laminar flow is one half of the maximum flow velocity.

2.5 Turbulent flow

According to Çengel & Cimbala (2017), turbulent flow is characterized by disorder and rapid fluctuations of swirling regions of fluid which are called eddies, throughout the flow. Eddies creates additional mechanism for the momentum and energy transfers in flow. Turbulent flow is associated with significant higher values of friction than laminar flow. This is due to the eddies transporting mass, momentum and energy more rapidly than molecular diffusion, resulting in enhanced mass, momentum and energy transfer. It is observed from Fig. 2.5 that if the instantaneous values of velocity are fluctuating around an average value, the velocity for turbulent flow can be expressed as a sum of an average value $\bar{u}$ and a fluctuating component u':

$$u = \bar{u} + u' \qquad (2.14)$$
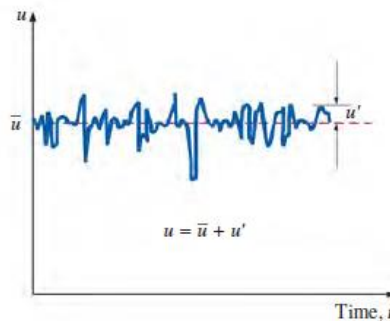
Figure 2.5 Fluctuations of the velocity component u as a function of time, (Çengel & Cimbala, 2017, p. 366)

This condition also applies to other parameters regarding turbulent flow, such as pressure $P = \bar{P} + P'$ and y-coordinate of the velocity $v = \bar{v} + v'$.

2.5.1 Turbulent shear stress

Experimental studies have shown that determining the shear stress in turbulent flow is not straight forward as in laminar flow. The turbulent shear stress can be considered as a combination of two components, a laminar component and a turbulent component:

$$\tau_{total} = \tau_{lam} + \tau_{turb} \tag{2.15}$$

where τ_{lam} is expressed as $\tau_{lam} = -\mu \, d\bar{u}/dr$ and τ_{turb} which accounts for the friction between the fluctuating fluid particles and the fluid body.

For determining the turbulent shear stress component τ_{turb}, it needs to be considered an upward eddy motion of a fluid particle from a layer of lower velocity through a differential area dA as a result of the velocity fluctuation v', as shown in Fig. 2.6.
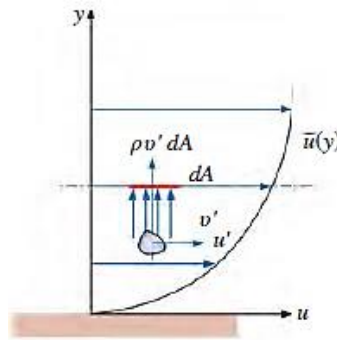
Figure 2.6 Fluid particle moving upward through a differential area dA as a result of the velocity fluctuating v', (Çengel & Cimbala, 2017, p. 366)

The mass flow rate of the fluid particle rising through dA is $\rho v' dA$, thus the momentum in the horizontal direction is $(\rho v' dA)u'$. Noting that the force in a given direction is equal to the rate of change in momentum in the specified direction, the horizontal force acting on a fluid element above dA due to the passage of fluid particles through dA is $\partial F = (\rho v' dA) - (u')$. From this, the shear force per unit area due to eddy motion of fluid particles $\partial F/dA = -\rho u' v'$ can be seen as the instantaneous turbulent shear stress. The turbulent shear stress can be expressed as:

$$\tau_{turb} = -\rho \overline{u'v'} \tag{2.16}$$

where $\overline{u'v'}$ is the time average of the product of the fluctuating component u' and v'. $-\rho \overline{u'v'}$ is also called Reynold stresses. (Çengel & Cimbala, 2017, p. 366)

2.5.2 Turbulent velocity profile

Turbulent velocity profiles are based on analysis and experimental data and are semi-empirical with constants acquired by the experimental data. The nearest layer to the wall is the viscous sublayer, where the viscous forces are dominant, and the velocity profile is nearly linear. Next to the viscous sublayer is the buffer layer. In the buffer layer the turbulent effects are becoming

significant, but flow is still dominated by viscous effects. Above the buffer layer, the overlap (or transition) layer is found, where the turbulent effects are more aggressive but still not dominant. The last layer is the outer layer, where viscous forces are overpowered by the turbulence effects. Due to all the different layers in a turbulent velocity profile, it is hard to analytically determine the whole velocity profile. The most optimal way to determine the turbulent velocity profile is to identify the key variables and functional form acquired by dimensional analysis, and to use experimental data to determine the numerical values of constants (Çengel & Cimbala, 2017, p. 368).

The viscous sublayer is thin, however it plays an important role on flow characteristics because of the high velocity gradients. The damping of the eddies makes the flow in the sublayer almost laminar and the shear stress consists of laminar shear stress component associated with the fluid viscosity. Since the velocity in the sublayer is nearly linear, and the velocity gradient $du/dy = 0$, the wall shear stress in the viscous sublayer can be expressed as:

$$\frac{\tau_w}{\rho} = \frac{\nu u}{y}$$

(2.17)

where y is the distance from the wall. The square root of τ_w/ρ has the dimensions of velocity, and thus it is appropriate to view it as a fictitious velocity called the friction velocity expressed as:

$$u^* = \sqrt{\frac{\tau_w}{\rho}}$$

(2.18)

Substituting Eq. (2.18) into Eq. (2.17), the dimensionless velocity profile of the viscous sublayer can be expressed:

$$\frac{u}{u^*} = \frac{yu^*}{\nu}$$

(2.19)

This equation is called the "law of the wall", and it is compared with experimental data and found to be satisfactory for smooth surfaces for $0 \leq yu^*/\nu \leq 5$.

From Eq. (2.19), the thickness of the viscous sublayer can be approximated:

$$y = \delta_{Sublayer} = \frac{5\nu}{u^*} = \frac{25\upsilon}{u_\delta} \tag{2.20}$$

where u_δ is the velocity at the end of the viscous sublayer ($u_\delta \approx 5u^*$). In boundary layer analysis, it is more convenient to work with non-dimensionalized distances and non-dimensionalized velocities, and therefore the non-dimensionalized distance y^+ and velocity u^+ are presented:

$$y^+ = \frac{yu^*}{\nu} \tag{2.21}$$

$$u^+ = \frac{u}{u^*} \tag{2.22}$$

Implementing the non-dimensional parameters into the Eq. (2.19), it becomes $y^+ = u^+$. The layer between the turbulent layer and buffer layer is called the overlap layer. The velocity in the overlap layer is found by experimental studies to line up as a straight line when plotted against the logarithmic distance from the wall. With previous dimensional analysis and experimental studies, it is confirmed that the velocity in the overlap layer is proportional with the logarithm of distance, and thus the equation for velocity can be expressed as:

$$\frac{u}{u^*} = \frac{1}{\kappa} \ln \frac{yu^*}{\nu} + B \tag{2.23}$$

where κ and B are constants determined by experimental studies to be $\kappa = 0.4$ and $B = 5.0$. Fig. 2.7 shows the comparison of the law of the wall and the logarithmic law. From the figure it can be observed that the logarithmic velocity profile is approximated accurate in the overlap layer from $y^+ > 30$. No good match is observed for the velocity profile in the range $5 < y^+ < 30$.
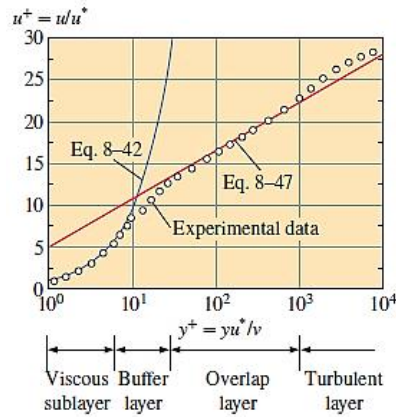
Figure 2.7 Comparison of the law of the wall and the logarithmic law (Çengel & Cimbala, 2017, p. 369)

For determining the velocity profile in the outer turbulent layer, the constant B is evaluated with respect to that the maximum velocity occurs in the middle of the pipe $r = 0$. Solving Eq. (2.23) for B and setting $y = R - r$ and $u = u_{max}$ gives:

$$\frac{u_{max} - u}{u^*} = 2.5 \, ln \frac{R}{R - r} \tag{2.24}$$

The term $u_{max} - u$ is called velocity defect, and is the deviation of the velocity from the velocity at the centerline $r = 0$, and thus Eq. (2.24) is named the velocity defect law. The relation in Eq. (2.24) shows that the velocity profile is dependent on the distance to the centerline of the flow and is independent of the viscosity of the fluid. This can be explained by the fact that the eddy motion is dominant in this region, causing the effect of the viscosity to be negligible.

For an empirical determination of the turbulent velocity profile, the most common is the power-law velocity profile:

$$\frac{u}{u_{max}} = \left(\frac{y}{R}\right)^{1/n} = \left(1 - \frac{r}{R}\right)^{1/n} \tag{2.25}$$

where the exponent n is a constant dependent on the Reynolds number, which is increasing with increase in Reynolds number. The power law profile cannot be used for calculating shear stress on the walls, as the velocity gradient in this region is of infinity. But since these regions of flow only constitutes for a small portion of the whole velocity profile, gives the power law velocity profile highly accurate results of turbulent flow in pipe. Fig. 2.8. shows the power law velocity

profile with different exponents n compared with the laminar parabolic velocity profile defined in Eq. (2.13).
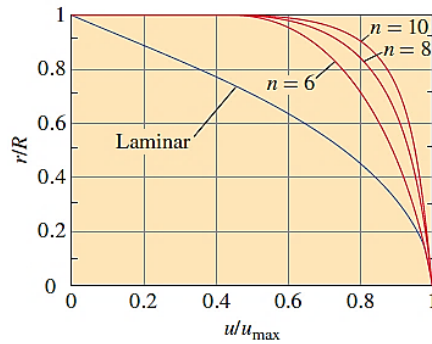
Figure 2.8 Power law velocity profile with different exponents n, compared with laminar parabolic velocity profile (Çengel & Cimbala, 2017, p. 370)

2.6 Orifice flowmeter

An orifice flow meter consists of a plate that has a sharp-edged hole in the middle, and is concentrically placed inside a pipe perpendicular to the flow direction. The pressure difference measured by the pressure tapping in the upstream and downstream of the flow is combined with the Bernoulli's equation to obtain the flow rate. Fig. 2.9. shows the locations of the pressure tappings denoted as section 1 and section 2.
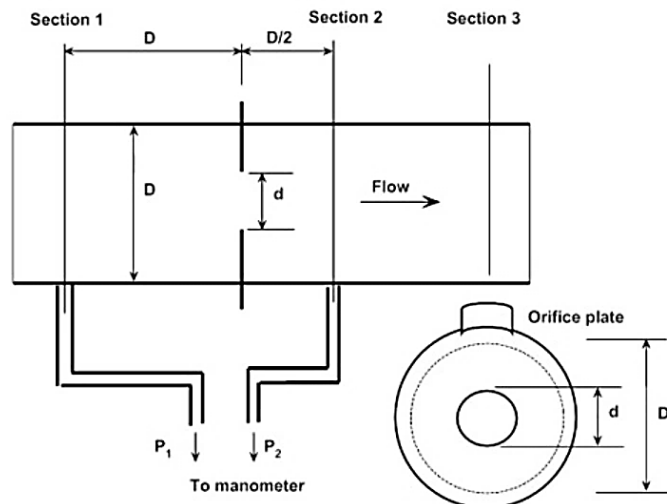
Figure 2.9 Schematic view of flow through an orifice plate and location of pressure tappings (Menon, 2015)

Consider an incompressible and steady flow inside a pipe with diameter D constricted to a flow with diameter d as shown in Fig. 2.9. According to Çengel & Cimbala (2017), the equation of mass balance and the Bernoulli's equation between section 1 and section 2 can be written as:

Mass balance:

$$\dot{Q} = A_1 V_1 = A_2 V_2 \rightarrow V_1 = (A_2/A_1)V_2 = (d/D)^2 V_2 \tag{2.26}$$

The Bernoulli's equation ($z_1 = z_2$):

$$\frac{P_1}{\rho g} + \frac{V_1^2}{2g} = \frac{P_2}{\rho g} + \frac{V_2^2}{2g} \tag{2.27}$$

Obstruction velocity can be obtained by combining Eq. (2.26) and Eq. (2.27) and solving for V_2:

$$V_2 = \sqrt{\frac{2(P_1 - P_2)}{\rho(1 - \beta^4)}} \tag{2.28}$$

where $\beta = d/D$ is the ratio between orifice diameter and pipe diameter. Eq. (2.28) is assumed to have no pressure loss, which is unrealistic as pressure loss due to frictional effects is inevitable. As a result, V_2 is overpredicted. To overcome this problem, a correction factor called the discharge coefficient C_d is implemented. Section 2.7 will introduce a more detailed explanation of the discharge coefficient. Obstruction flow rate with the factor of discharge is given as:

$$\dot{Q} = A_0 C_d \sqrt{\frac{2(P_1 - P_2)}{\rho(1 - \beta^4)}} \tag{2.29}$$

where $A_0 = A_2 = \pi d^2/4$ is the cross-sectional area of the circular orifice.

2.7 Discharge coefficient

According to Çengel & Cimbala (2017), the physical meaning of the discharge coefficient is the ratio between actual- and theoretical flow rate. As mentioned in Section 2.6, the discharge coefficient is a correction factor to modify the flow rate calculation by using the correction factor to cover the pressure loss due to the frictional effects. The discharge coefficient is determined by conducting experimental or numerical studies, and it is found that the coefficient is dependent on β and Re. The discharge coefficient can be expressed as follows:

$$C_d = \frac{1}{2\sqrt{2}} \left(\frac{1}{\beta}\right)^2 (1 - \beta^4)^{\frac{1}{2}} \frac{1}{\sqrt{\Delta P^*}} \tag{2.30}$$

where $\Delta P^* = (P_1 - P_2)/u_{max}^2$, P_1, P_2 is pressure at section 1 and 2 as shown in Fig. 2.9, and u_{max} is the maximum velocity of the flow, at the location of $r = 0$.

Curve fitting correlations for C_d are available for different types of obstruction flowmeters. Miller (1997) conducted experimental studies on standardized flowmeter geometries, and gave a relationship between β and C_d for the orifice flowmeter as:

$$C_d = 0.5959 + 0.0312\beta^{2.1} - 0.184\beta^8 + \frac{91.71\beta^{2.5}}{Re^{0.75}} \tag{2.31}$$

Miller (1997) found that this relation is valid for $0.25 < \beta < 0.75$ and $10^4 < Re < 10^7$. However, this relation is not suitable for precise values of C_d because different obstruction design parameters may have an impact on the values.

Chapter 3 Computational Fluid Dynamics

A brief introduction to Computational Fluid Dynamics and the CFD code OpenFOAM are presented in present chapter. The theory of the finite volume method and OpenFOAM discretization are also introduced.

3.1 Introduction to Computational Fluid Dynamics

Computational Fluid Dynamics (CFD) is a powerful method that gives a qualitative prediction of a flow field using numerical simulations and the codes are continuously improved. CFD was first used in the field of aerodynamic research, but quickly developed into other engineering areas such as marine- and offshore technology.

Several CFD codes have been developed over the years, both licensed and open source. Still, almost all CFD codes follows a similar three-steps procedure for solving a problem:

Pre-processing: The pre-processing is done by defining the geometries, the boundary conditions, physical parameters and generating a mesh of the computational domain.

Solving: Solving is done by selecting appropriate solvers implemented in the CFD codes. The solver calculates the flow variables stored in nodes inside a cell in the pre-defined mesh, which is further explained in Section 3.4.

Post-processing: The numerical results are processed using different post-processing tools. This can be done for processing the output data for flow variables, or by visualizing the flow.

3.2 OpenFOAM

OpenFOAM, short for Open Field Operation And Manipulation, is an open source software package written in C++. It is used to solve problems within the field of fluid mechanics as Computational Fluid Dynamics, but can also be used for solving problems within solid mechanics. OpenFOAM is a finite volume method-based solver (Moukalled, 2015), a numerical method for solving partial differential equations and calculates the regarding

variables averaged over a cell volume defined in a pre-made mesh, which is further explained in Section 3.4.

To use OpenFOAM, the user needs to create a case directory folder with three subfolders: "0" folder for defining the initial conditions and the boundary conditions for the variables, "constant" folder for the information of the mesh and physical properties, and "system" folder containing the information about the numerical schemes and methods of solving the system of linear algebra equations. Fig. 3.1 illustrates a typical case directory structure in OpenFOAM.
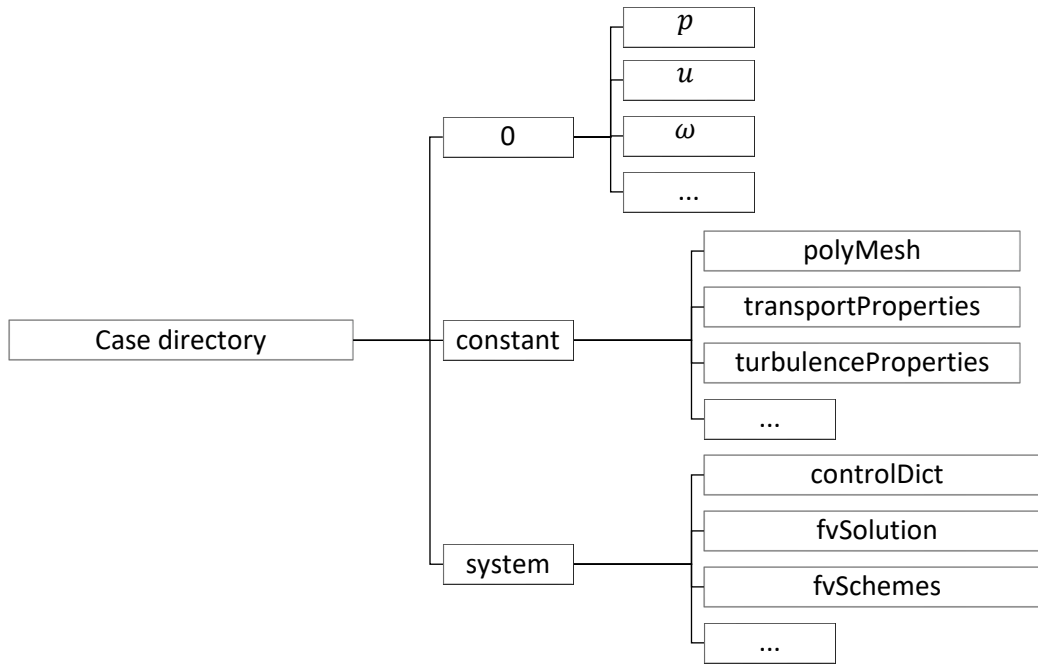
Figure 3.1 Case directory structure in OpenFOAM

3.3 Governing equations

In the present study, the flow is assumed to be incompressible and viscous. The governing equations are the Navier-Stokes equations which includes the continuity equation and the momentum conservation equations, given by:

$$\frac{\partial u_i}{\partial x_i} = 0 \tag{3.1}$$

$$\frac{\partial u_i}{\partial t} + u_j \frac{\partial u_i}{\partial x_j} = -\frac{1}{\rho} \frac{\partial p}{\partial x_i} + \nu \frac{\partial^2 u_i}{\partial x_j \partial x_j} \tag{3.2}$$

Where $i, j = 1,2,3$. x_1, x_2, x_3 denote the streamwise and the two-cross-stream directions, respectively and u_1, u_2, u_3 are the corresponding velocity components. p is the pressure and ρ is the density of the fluid.

3.4 The finite volume method

In fluid dynamics, it is important that the conservation laws in integral form are presented precisely. The most appropriate way to accomplish this, is to discretize the integral forms of the equations, which is the basis of the finite volume method. The flow domain is divided into a set of non-overlapping cells, called control volumes, that cover the whole domain. The conservation laws are applied to discrete points, called nodes, in the cells to determine the flow variables (Author Dick E. in Wendt, 2009). These discrete points are normally located in the cell-centers, cell-vertices or cell mid-sides. Fig 3.2 illustrates a control volume, where P denotes the discrete points (also called computational points) in the control volume, f denotes the face of the control volume, S denotes the surface normal vector and N is the discrete point in the neighboring cell (Jasak, 1996, p. 75).
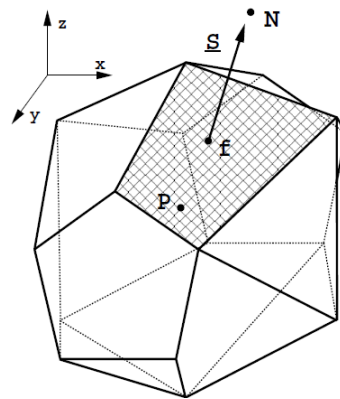
Figure 3.2 Example of control volume (Jasak, 1996, p. 75)

The divided domain forms a grid that can be split into two main categories: Structured and un-structured grid. Fig. 3.3 shows examples of a structured grid and an un-structured grid. A structured grid consists of ordered planar cells with four edges (2D) or with six faces (3D), and each cell is numbered according to the indices (*i, j, k*). An un-structured grid consists of cells of various shapes, and the cells cannot be identified by the indices and thus is numbered in another manner inside the CFD code. One of the main advantages of using a structured mesh is

that it often is better for refinement in boundary layer flow close to the walls compared to unstructured grid with the same number of cells.
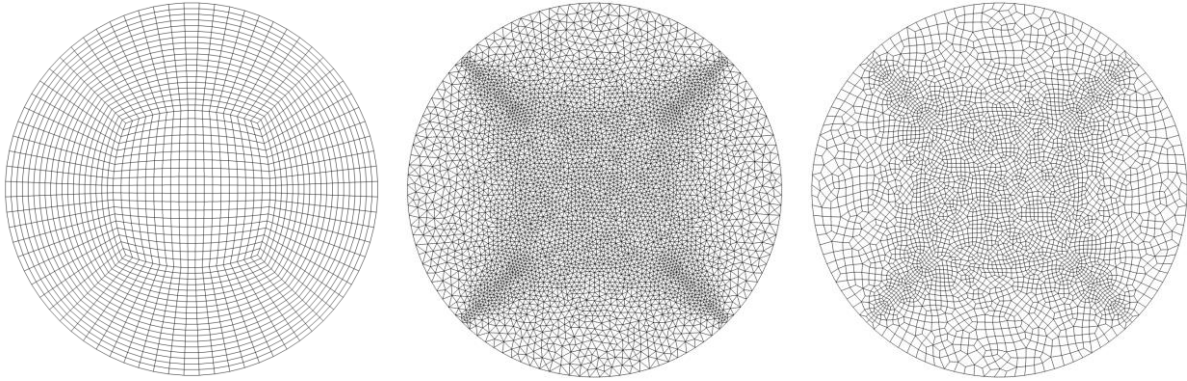
Figure 3.3 From left to right: Structured quadrilateral grid, Un-structured triangular grid, Un-structured quadrilateral grid

3.5 OpenFOAM discretization

This section describes how the transport equation is discretised in OpenFOAM and the associated schemes that are used in the present study. Theory of the discretization is based on the text of Jasak (1996).

The transport equation for a scalar ϕ that can represent pressure or a velocity component can be written as:

$$\frac{\partial \rho \phi}{\partial t} + \nabla.(\rho U \phi) - \nabla.(\rho \Gamma_\phi \nabla \phi) = S_\phi(\phi) \tag{3.1}$$

where $\partial \rho \phi / \partial t$ is the temporal derivative, $\nabla.(\rho U \phi)$ is the convection term, $\nabla.(\rho \Gamma_\phi \nabla \phi)$ is the diffusion term and $S_\phi(\phi)$ is the source term. As mentioned in Section 3.4, it is important that the integral form of the transport equation is accurately defined over the control volume V_P around the point P. The integral form of the transport equation defined in Eq. (3.1) can be written as (Jasak, 1996):

$$\int_t^{t+\Delta t} \left[\frac{\partial}{\partial t} \int_{V_P} \rho \phi \, dV + \int_{V_P} \nabla.(\rho U \phi) \, dV - \int_{V_P} \nabla.(\rho \Gamma_\phi \nabla \phi) \, dV \right] dt$$

$$= \int_t^{t+\Delta t} \int_{V_P} \left(S_\phi(\phi) \, dV \right) dt \tag{3.2}$$

Eq. (3.2) is further discretized and divided into two sub-categories: Spatial and temporal discretization. This is further described below.

3.5.1 Spatial discretization

The general discretization integrals for a control volume V_P are discussed in this section. For a more comprehensive elaboration of the spatial discretization, see Jasak (1996, p.78-87).

Gauss' theorem in discretized second-order form is given:

$$(\nabla . \phi)V_P = \sum_f S . \phi_f \tag{3.3}$$

where f is the value of the variable ϕ, and S is the face area vector.

Discretization of convective term

From Eq. (3.3), the discretized convective term can be obtained:

$$\int_{V_P} \nabla . (\rho U \phi)dV = \sum_f S . (\rho U \phi)_f = \sum_f F \phi_f \tag{3.4}$$

where F is the mass flux, defined as $F = S . (\rho U)_f$. The flux is calculated from interpolated values of ρ and U between two neighbouring cell values P.

Discretization of diffusion term

Assuming linear variation of ϕ and implementing this into Eq. (3.3) obtains the discretized diffusion term:

$$\int_{V_P} \nabla . (\rho \Gamma_\phi \nabla \phi)dV = \sum_f S . (\rho \Gamma_\phi \nabla \phi)_f = \sum_f (\rho \Gamma_\phi)_f S . (\nabla \phi)_f \tag{3.5}$$

If the mesh is orthogonal, the discretized diffusion term can be defined as follows:

$$S . (\nabla \phi)_f = |S| \frac{\phi_N - \phi_P}{|d|} \tag{3.6}$$

Where P and N are neighboring cells, and S and d are the vectors that are parallel to each other for such meshes. An additional term is included for the non-orthogonal correction:

$$S . (\nabla \phi)_f = |S| \frac{\phi_N - \phi_P}{|d|} + S_\Delta(\overline{\nabla \phi}) \tag{3.7}$$

It can be shown from Eq. (3.7) that high non-orthogonality can result in negative coefficients, which can lead to reduced accuracy in results. This indicated the importance of limiting the non-orthogonality when generating a mesh.

OpenFOAM provides a large variety of spatial schemes for handling derivatives and interpolation of values between points. Table 3.1 shows the different spatial schemes used in present study. The schemes are based on the Gaussian finite volume integration, where the resulting values on the faces are interpolated from the cell centres.

Table 3.1 Spatial schemes used in present study. All schemes are second-order accurate

Term	Scheme
Gradient ∇	Gauss linear
Divergence $\nabla\cdot$	Bounded Gauss upwind
Laplacian ∇^2	Gauss linear corrected
Interpolation	Linear

3.5.2 Temporal discretization

In same manner as in spatial discretization, OpenFOAM has several different methods for discretizing time. The temporal scheme used in present study for all simulations are the Euler implicit time scheme. The Euler scheme is a first order implicit time scheme used for transient flow. The scheme can be written in the form:

$$\phi_f = f_x\,\phi_P^n + (1 - f_x)\phi_N^n \qquad (3.8)$$

where f_x is the linear interpolation factor.

$$S\,(\nabla\phi)_f = |\Delta|\frac{\phi_N^n - \phi_P^n}{|x|} + \kappa\,(\nabla\phi)_f \qquad (3.9)$$

where S is the surface normal vector, κ is the vector orthogonal to the normal surface vector S.

To keep the present simulations stable and temporal diffusion to a minimum, a maximum allowable Courant number of $Co = 0.8$ is used for all present simulations. The Courant-Friedrichs-Lewy condition, written as the CFL conditions, is a numerical stability criterion for hyperbolic equations. The equation for CFL criterion can be written as:

$$Co = |u|\frac{\Delta t}{\Delta x} \leq 1 \tag{3.10}$$

where $|u|$ is the magnitude of the flow velocity at the considered location, Δt is the maximum timestep interval and Δx is the grid cell length. For the solution to be stable and converged, Δt must be small enough to ensure that the $|u|/\Delta x$ does not exceed 1.

3.5.3 Numerical solver

In all present simulations, the solver pimpleFoam is used. pimpleFoam is based on the PIMPLE algorithm implemented in OpenFOAM, and is one of the most widely used solvers for transient flow. The PIMPLE algorithm combines the benefits of the PISO (Pressure-Implicit Splitting-Operator) and the SIMPLE (Semi-Implicit Method for Pressure-linked equations) algorithm into one algorithm. The PIMPLE algorithm uses outer correction loops, which defines how many iterations to be performed on the system of equations. Outer corrector loops are enabled to ensure that the explicit parts of the equations are converged. If no outer corrector loops are used, the algorithm is equivalent to the PISO algorithm (Holzman, 2017, p-115). The PIMPLE algorithm allows a dynamic time step method, enabling the user to use an adjustable time step with respect to a maximum allowable Courant number. In all present simulations, the adjustable time step utility is used with the maximum allowable Courant number of $Co = 0.8$. Fig. 3.4 shows a simplified flowchart of the PIMPLE algorithm.
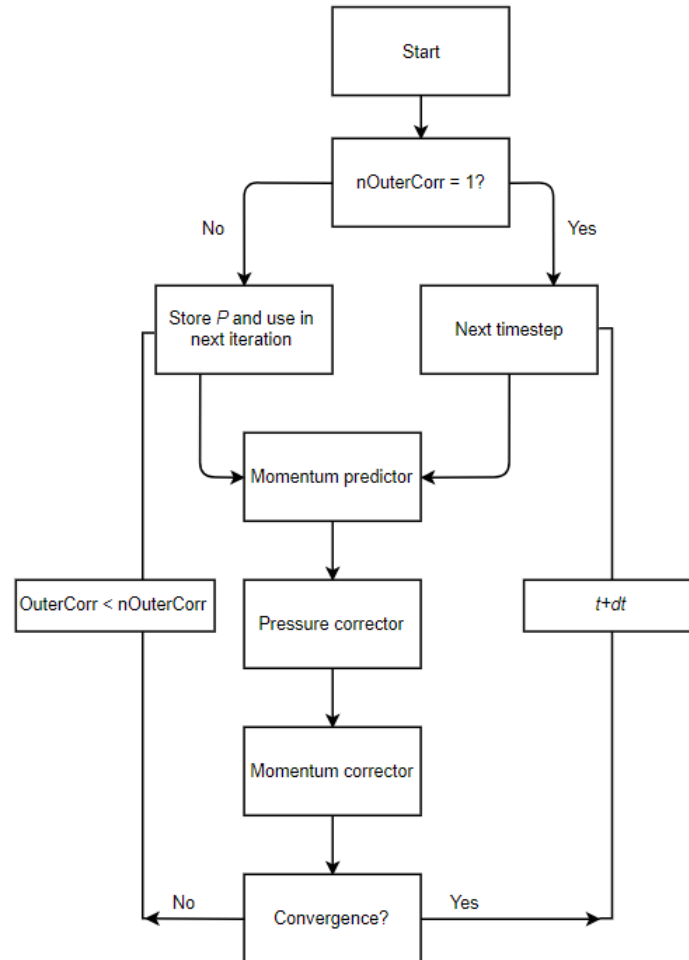
Figure 3.4 Flowchart of the PIMPLE algorithm. nOutercorr is the number of outer corrector loops.

3.6 Turbulence modeling

This section will cover the modeling of turbulence in OpenFOAM. The theory behind turbulent flow is described in Section 2.5.

3.6.1 k-ω SST turbulence model

In this study, the Shear Stress Transport k-ω turbulence model is used (Menter, 1994), known as k-ω SST. The k-ω SST turbulence model is one of the most used turbulence models, and is proficient for predicting adverse pressure gradient boundary layers and flow separation. The k-ω SST model is a combination of the k-ω turbulence model by Wilcox (1988) and the k-ε turbulence model created by Launder & Spalding (1972), where it attempts to apply the k-ω

model to the regions near surface and apply the k- ε model to outer boundary layers and the free shear layers. In the k-ω SST model, the transport equations for turbulent kinetic energy k and specific dissipation rate ω can be represented as:

$$\rho \frac{\partial k}{\partial t} + \rho u_j \frac{\partial k}{\partial x_j} = \frac{\partial}{\partial x_j}\left(\left(\mu + \frac{\mu_t}{\sigma_k}\right)\frac{\partial k}{\partial x_j}\right) + G_k - Y_k \tag{3.11}$$

$$\rho \frac{\partial \omega}{\partial t} + \rho u_j \frac{\partial \omega}{\partial x_j} = \frac{\partial}{\partial x_j}\left(\left(\mu + \frac{\mu_t}{\sigma_\omega}\right)\frac{\partial \omega}{\partial x_j}\right) + G_\omega - Y_\omega + D_\omega \tag{3.12}$$

where G_ω and G_k express the development of k and ω due to the mean velocity gradients, Y_ω and Y_k express the dissipation of k and ω and D_ω represent the cross-diffusion term. The turbulent viscosity μ_t can be expressed as:

$$\mu_t = \frac{\alpha \rho k}{\omega} \tag{3.13}$$

where α is a constant.

Chapter 4 Laminar flow through a square edged orifice inside a pipe

This chapter presents the computational grid and numerical setup used in the numerical investigation of laminar flow through a square edged orifice inside a pipe. This includes a grid convergence study on the generated mesh and a validation study of the obtained results. Firstly, a validation of the boundary conditions and control parameters are done by the numerical investigation of the fully developed parabolic velocity profile inside a straight pipe without an orifice, and compared with a theoretical solution obtained from Eq. (2.13.). Furthermore, the validation study of the pipe with orifice is carried out by comparing the present calculated discharge coefficient with the previous published numerical and experimental results. The effect of the Reynolds number, thickness of the orifice to pipe diameter ratio t and orifice diameter to pipe diameter ratio β on the flow are discussed based on the velocity, streamline and Q-criterion contours. The content in this chapter covers the part of simulations and results from **Paper 1** in appendix.

4.1 Pre-processing

The pre-processing of the numerical simulations is done by defining the boundary conditions and control parameters, and generating a mesh of the geometry.

The computational domain consists of a circular, square edged orifice inserted at *L/2* inside a pipe with a diameter of D =1 m as shown in Fig. 4.1. The pipe length is set to be $L = 10\ D$ without the additional length from the orifice thickness.
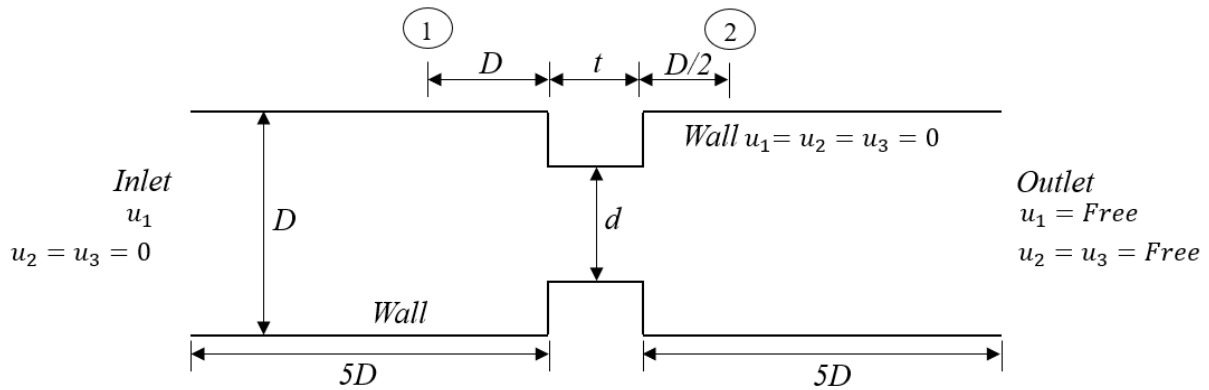
Figure 4.1. Computational domain

The boundary conditions for the flow in the pipe are as follows:

Inlet: At the inlet, parabolic laminar velocity profile (Eq.2.13) $u_1 = 2\ u_{Avg}[(1\text{-}r/R)^2]\ u_2 = 0, u_3 = 0$ is prescribed, and the pressure is set to be zero normal gradient. u_{Avg} is set to be 1 *m/s*.

where u_{Avg} is the average flow velocity, r is the distance to the pipe center and R is the radius of the pipe.

Outlet: At the outlet, the velocity is set as zero normal gradient and the pressure is set to be zero.

Walls: On the walls of the pipe and the orifice plates, no-slip boundary condition is used for the velocities $u_1 = u_2 = u_3 = 0$ and the pressure is set to be zero normal gradient.

4.2 Validation of boundary conditions and control parameters

To ensure that the boundary conditions and control parameters in this investigation are properly defined, a straight pipe convergence and validation study are performed. The boundary conditions used in this study are the same as defined in Section 4.1, and the flow is laminar at $Re = 1000$. Three meshes with different grid resolutions are used as shown in Table 4.1, and the simulated results are compared against the analytical solution obtained from Eq. (2.13). Fig. 4.2 shows the grids alongside and inside the pipe of Mesh 1. From Fig. 4.3 it can be observed that all grid resolutions are converged and are in good agreement with the analytical solution for the streamwise velocity profile. The streamwise velocity profiles at different streamwise locations, shown in Fig. 4.4, are in good agreement with each other. It can be determined from these results that the boundary conditions and control parameters are properly defined and can be used for further investigation of the flow inside an orifice plate.

Table 4.1 Cases in convergence study of straight pipe with different grid resolutions

Mesh	Grid resolution
Mesh 1	90 250
Mesh 2	203 125
Mesh 3	312 325
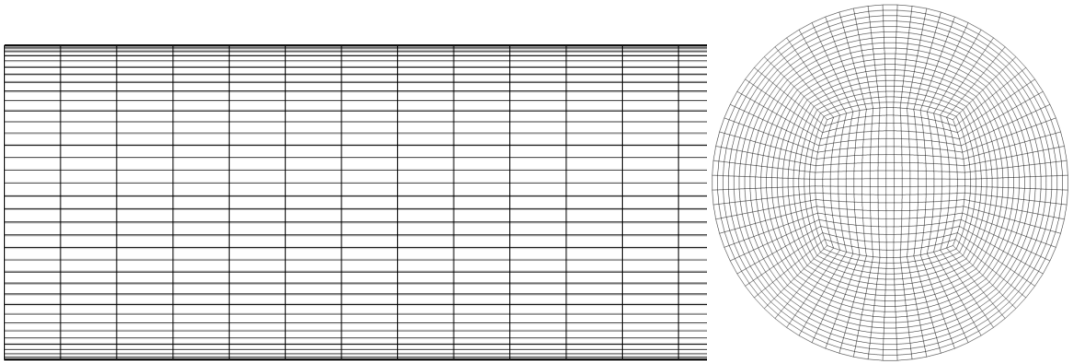
Figure 4.2 Grid alongside and inside the straight pipe of Mesh 1.
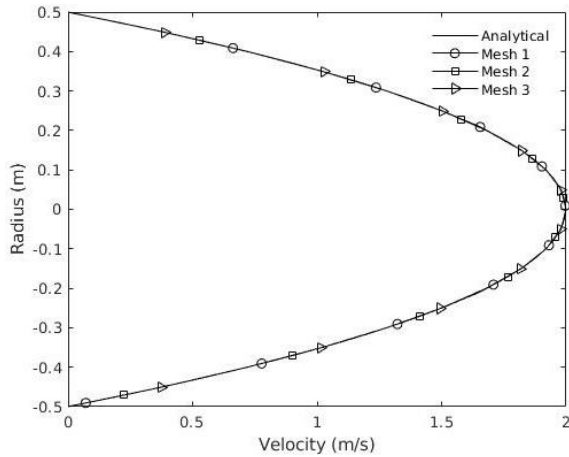
Figure 4.3 Streamwise velocity profile for three different grid resolutions compared with the analytical solution
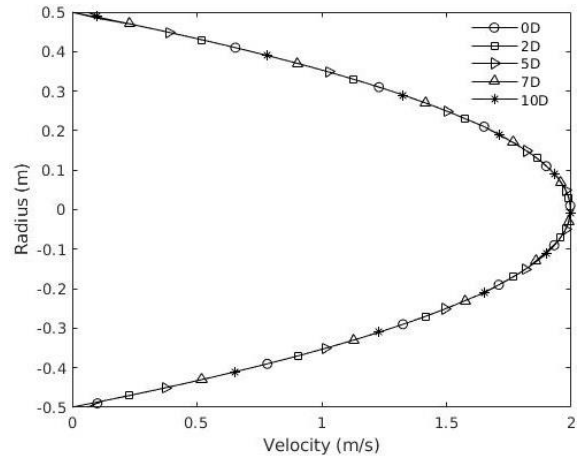
Figure 4.4 Streamwise velocity profile at different streamwise locations inside the pipe for Mesh 1

4.3 Convergence study

The computational grids for the orifice in the axis and cross section directions of the present study are shown in Fig 4.5. The grids in the axis direction are refined near the orifice plate. To ensure that the simulation results are fully converged inside the pipe, a grid convergence study is carried out. Four grid resolutions from coarse to fine are selected. Fig 4.6 shows the pressure distributions $P^* = p/\rho$ along the pipe axis for different grid resolutions and Table 4.2 presents the relative differences in the pressure through the orifice with the finest grid of Mesh 4.
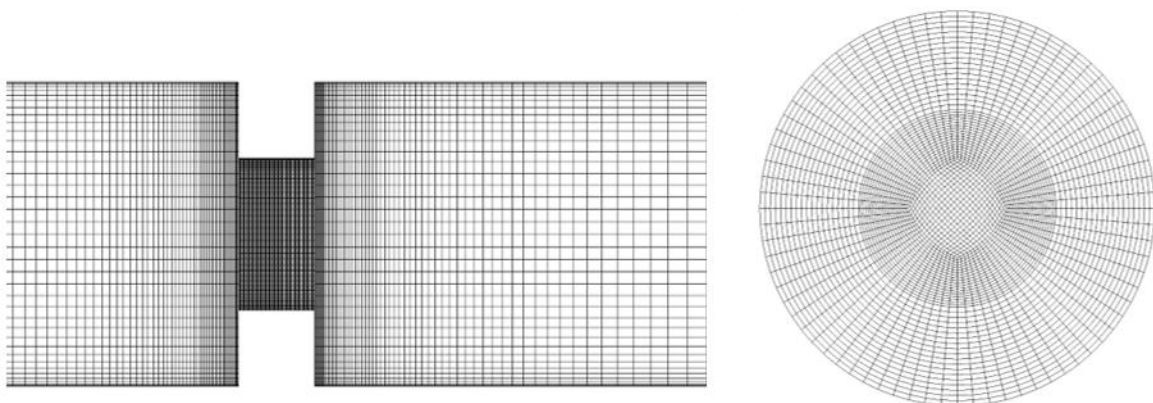
Figure 4.5 Example of Mesh 2, $\beta = 0.5$ and t=0.5, around orifice region and grid inside pipe

Table 4.2 Results of the cases in convergence study with different grid resolution

Case	Elements	Mean deviance from Mesh 4
Mesh 1	404 320	20.949%
Mesh 2	968 968	0.344%
Mesh 3	2 303 120	0.092%
Mesh 4	3 040 552	-
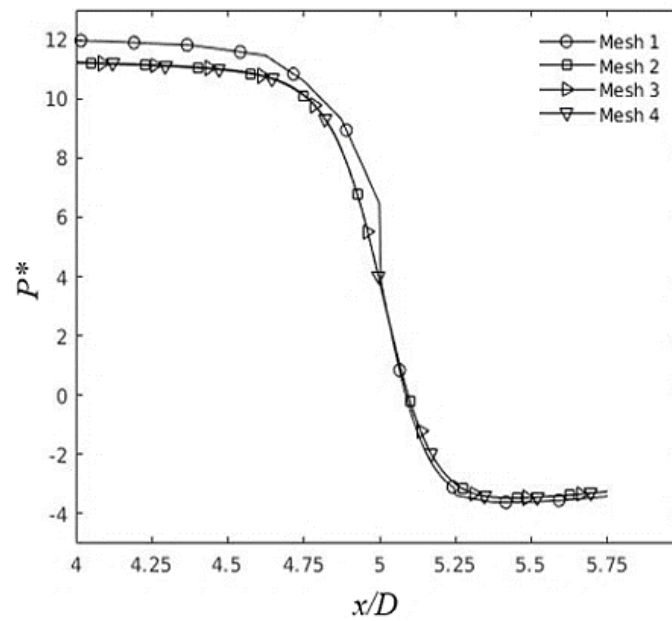
Figure 4.6 Pressure distribution through orifice

It is shown that there is negligible difference in the pressures among Mesh 2,3,4 and Mesh 2 is sufficient to produce fully converged results. Taking the computational amount into consideration, the grid resolution of Mesh 2 is chosen for the whole simulation in the present study for laminar flow.

4.4 Results and discussion

In this section, the results obtained from the numerical simulations of laminar flow through a straight pipe with a square edged orifice plate are presented. In section 4.4.1, calculated discharge coefficient for cases with variable thickness are compared against previous experimental and numerical study and discussed. In section 4.4.2, calculated discharge coefficients for orifice with variable β are presented and the trends of the discharge coefficients are discussed. In section 4.4.3, 4.4.4 and 4.4.5, the effects of altering the Reynolds number Re, orifice diameter to pipe diameter β and orifice thickness t on the flow characteristics are discussed by presenting the streamwise velocity, streamlines and Q-criterion contour plots.

4.4.1 Validation study

Validation of the results is carried out by comparing the discharge coefficient (Eq. 2.13) obtained from the numerical results for different orifice thickness at different Reynolds numbers with previous numerical and experimental data obtained by Sahin & Ceyhan (1996).

The discharge coefficient is a function of orifice diameter to pipe diameter ratio β, and pressure loss through the orifice $\Delta p = p_1^* - p_2^*$, where p_1^* is pressure measured at probe location 1 and p_2^* is pressure measured at probe location 2 as shown in Fig. 4.1. The parameters and the grids numbers for validation are shown in Table 4.3. The results of the present study are compared with published data in Fig. 4.7. In general, the present results are in good agreement with the experimental and numerical data of Sahin & Ceyhan (1996). For large t at high Reynolds number, the present results are in good agreement with the data of Sahin & Ceyhan (1996). For small t in Fig. 4.8 (a), (b), the present results are slightly higher than the experimental and numerical data of Sahin & Ceyhan (1996). There are underestimations at $Re = 16$ for $t = 0.125$ and at $Re = 4$ for $t = 0.25$. Further comparisons are made for different t at $Re = 100$ in Table 4.4. It can be seen that for smaller t, there is approximately 4.35% difference in the present results from the those of the previous numerical simulations and 6% from the experimental results.

Table 4.3 Cases in validation study of straight pipe with an orifice

Case	β	t	Cells
1	0.5	0.125	1 128 560
2	0.5	0.25	993 282
3	0.5	0.5	968 968
4	0,5	1	1 011 520
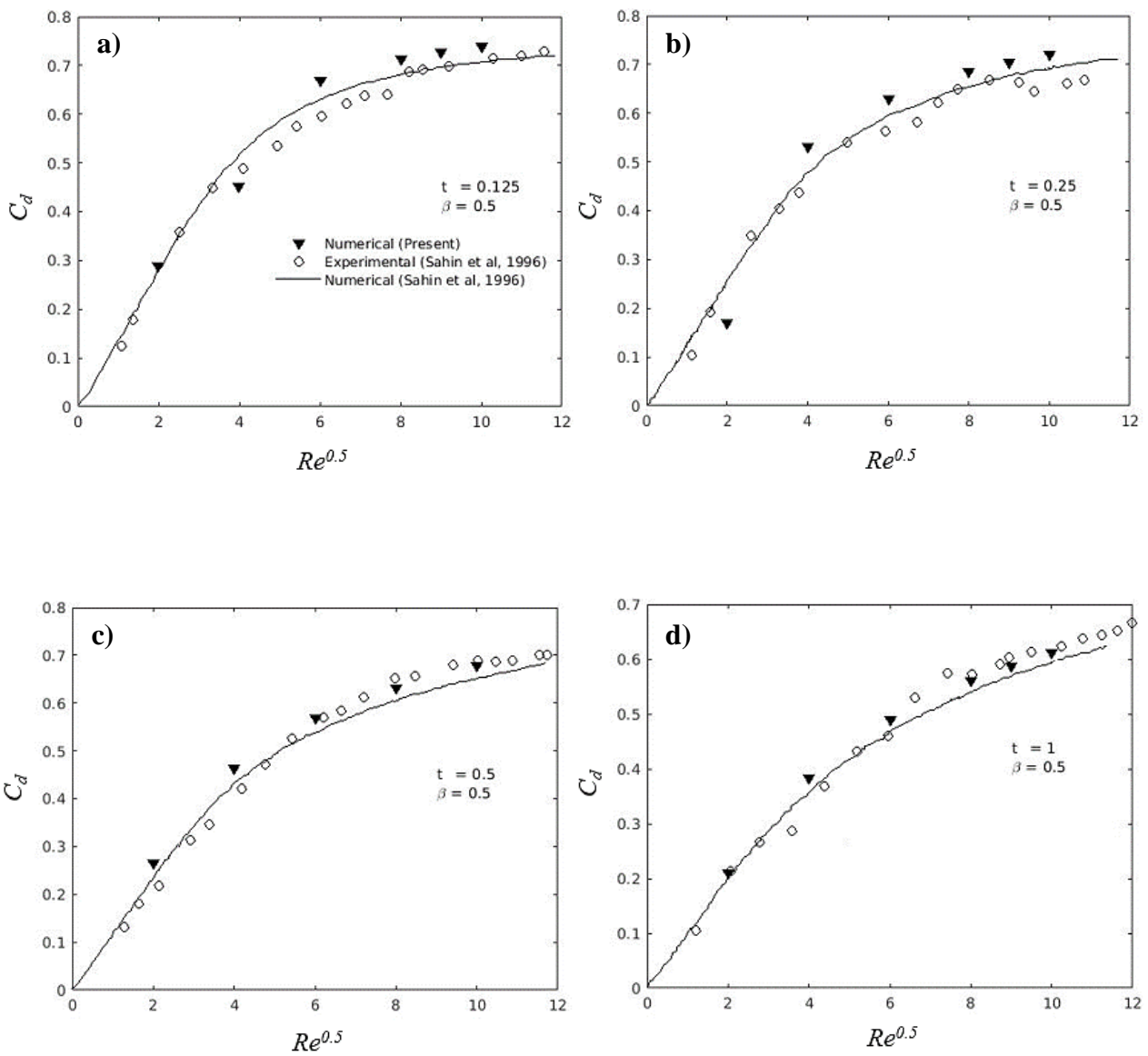
Figure 4.7 Variation of discharge coefficients with increasing Reynolds number, compared with results from Sahin & Ceyhan, 1996

Table 4.4 Validation of present numerical results compared with numerical and experimental results by Sahin & Ceyhan (1996)

No.	Author	Re	t	Numerical C_d	Experimental C_d
1	Present	100	0.125	0.7374	
2		100	0.25	0.7207	
3		100	0.5	0.6765	
4		100	1	0.6115	
5	Sahin & Ceyhan (1996)	100	0.125	0.7061	0.7155
6		100	0.25	0.6887	0.6614
7		100	0.5	0.6506	0.6900
8		100	1	0.5950	0.6223

4.4.2 Discharge coefficient

Effects of different orifice characteristics on the discharge coefficient are discussed. The discharge coefficients of the present numerical simulations with variation of Reynolds number are shown in Fig. 4.8, and the values are listed in Table 4.6. It can be observed for Case 5 the discharge coefficient increases aggressively from $0 \leq Re \leq 100$, and starts to be stable at $Re \geq$ 100. It is worth mentioned that due to the small orifice diameter in Case 5, the acceleration of the flow after passing the orifice may cause weak turbulent flow. For Case 6 and Case 7, it can be observed that the discharge coefficient increases less rapid than that of Case 5 at $0 \leq Re \leq$ 100, and is still increasing from $Re = 400$. The larger β causes less restriction to the flow passing through the orifice, and the pressure drop is not so significant as that in Case 5.

Table 4.5 Overview of the cases in present study

Case	β	t	Cells
5	0.25	0.25	1 128 560
6	0.75	0.25	993 282
7	0.5	2	1 282 080
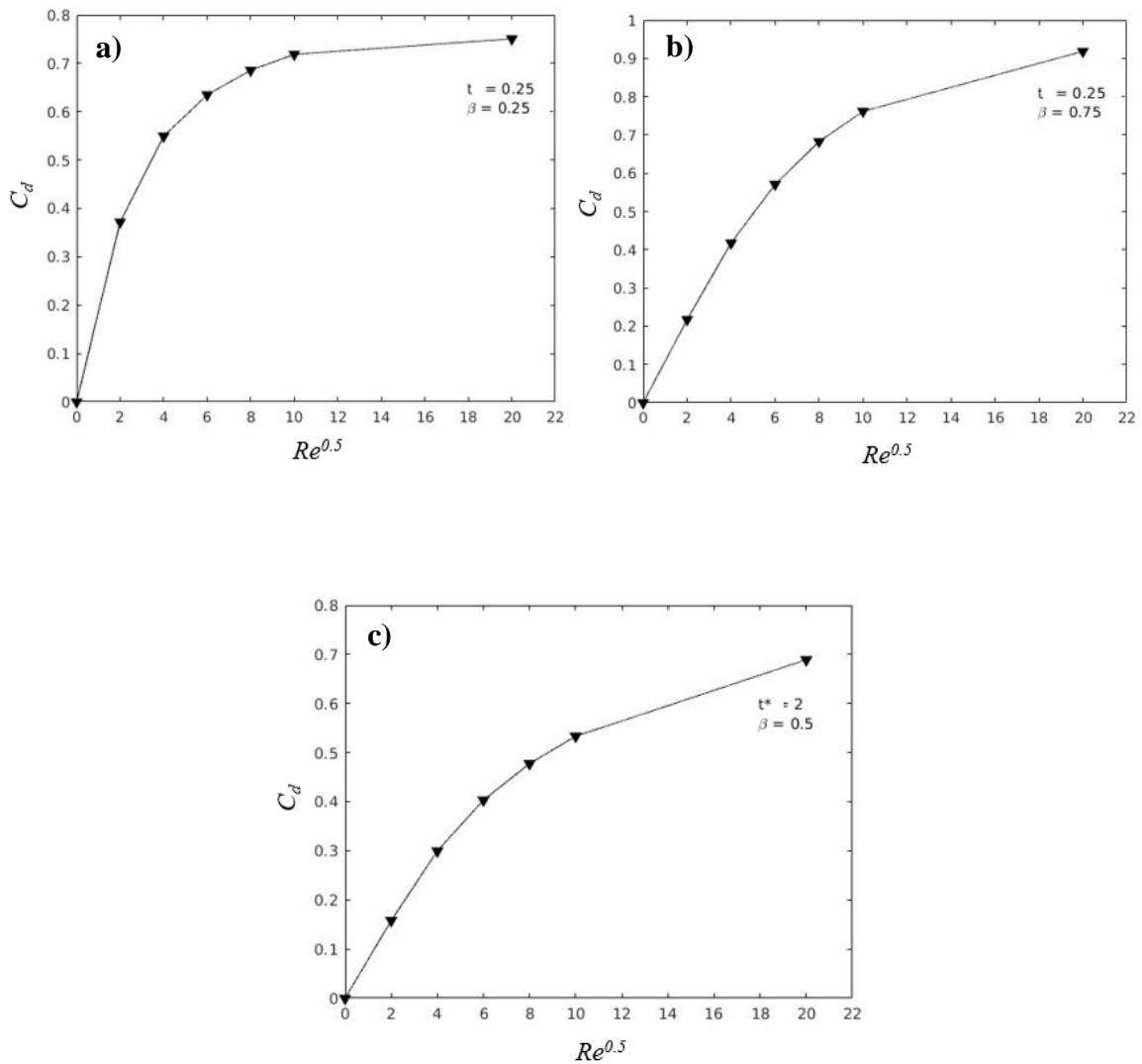
Figure 4.8 Variation of discharge coefficients with increasing Reynolds numbers for a) Case 5, b) Case 6, c) Case 7

Table 4.6 Discharge coefficients at different Reynolds numbers for different orifice characteristics

Case	β	t	C_d	C_d	C_d	C_d	C_d	C_d
			$Re=4$	$Re=16$	$Re=36$	$Re=64$	$Re=100$	$Re=400$
5	0.25	0.25	0.3718	0.5493	0.6350	0.6857	0.7185	0.7508
6	0.75	0.25	0.2174	0.4175	0.5708	0.6823	0.7615	0.9184
7	0.5	2	0.1581	0.2997	0.4033	0.4774	0.5333	0.7652

4.4.3 Effect of Reynolds number on flow characteristics

Streamwise velocity contours, streamlines and Q-criterion contours of Case 5 at Re= 16, 64, 100 are presented in Fig. 4.9. From the streamwise velocity contours, it can be seen that the flow is accelerated from a distance before the orifice plate and this is more prominent with increasing Re. Compression of the flow can be observed when the flow enters the orifice, and after the orifice, the flow appears to be a jet. The jet flow expansion is observed to shrink at higher Re, and the length of the jet is increased.

The streamlines in front of the orifice keep attached to the orifice because of the low Re, and are compressed when entering the orifice. In the outlet of the orifice, recirculation of the streamlines occurs, and the flow quickly re-attach to the pipe wall at lower Re. The recirculation length becomes larger at higher Re.

The Q criterion is used to identify the vortical structures (Hunt et al. 1988), which is defined as

$$Q = \frac{1}{2}[|\Omega|^2 - |S|^2] > 0 \tag{4.1}$$

Where $\Omega = \frac{1}{2}\left(\frac{\partial u_i}{\partial x_j} - \frac{\partial u_j}{\partial x_i}\right)$ is the rotation tensor and $S = \frac{1}{2}\left(\frac{\partial u_i}{\partial x_j} + \frac{\partial u_j}{\partial x_i}\right)$ is the strain tensor.

It can be observed that vortical structures form both inside and after the orifice. The vortical structures inside the orifice tend to be tilted in the streamwise direction, and the vortical structure after the orifice tends to locate in the fringe of the recirculation motions. The strength of the vortical structures reduces with increasing Re, which is due to the increasing rate of strain in the flow with increasing Re.

a)

b)

c)
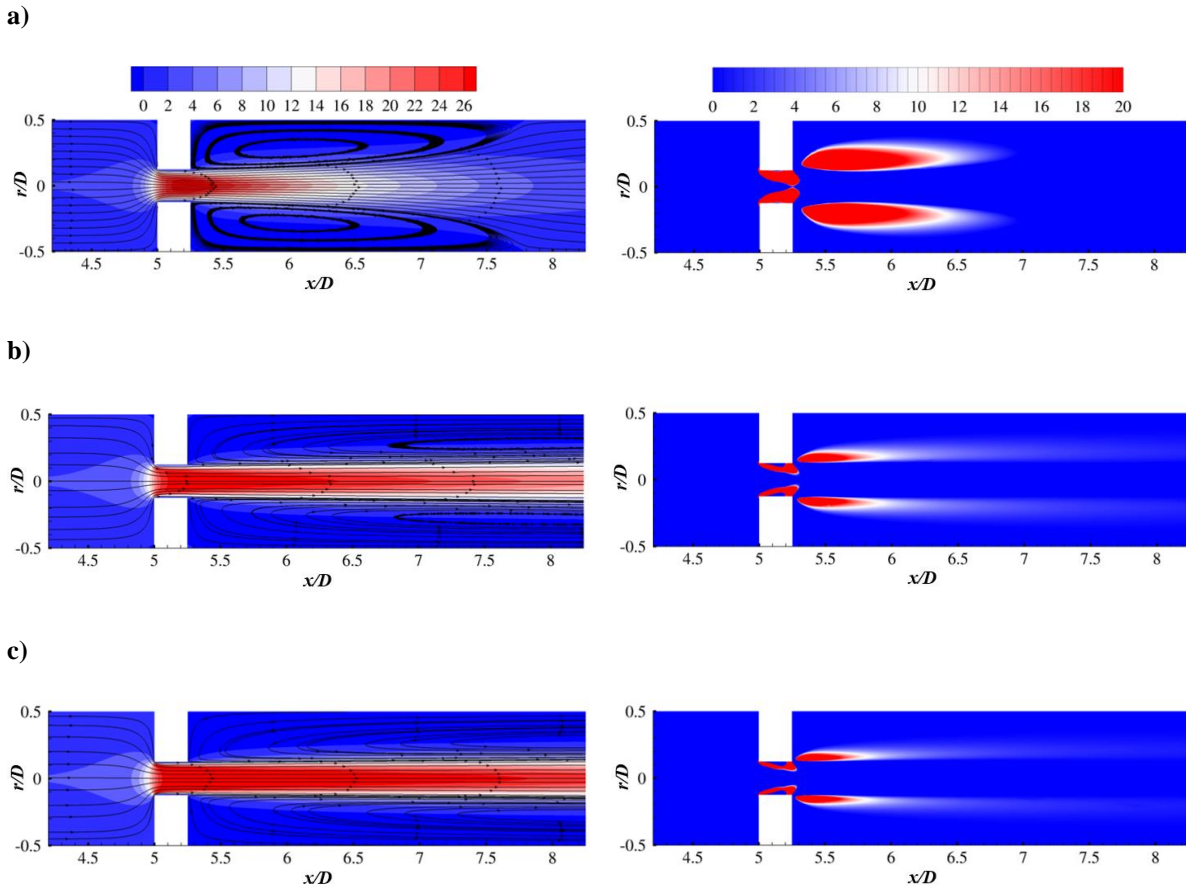
Figure. 4.9 Streamwise velocity contours, streamlines and Q-criterion contours for Case 5, (a) Re =16, (b) Re = 64 and (c) Re = 100.

4.4.4 Effect of β on flow characteristics

Table 4.7 shows the recirculation length with varying β at Re = 16 as an example. Flow recirculation occurs from the inlet of the orifice plate due to the adverse pressure gradient, and the recirculation length is the distance between the point of separation and the point of the flow re-attachment (Kundu & Cohen, 2008, p.382). The recirculation length decreases with increasing β. Further comparisons are made for streamwise velocity contours, streamlines as well as Q criterion contours at Re = 100. From the streamwise velocity contours, the acceleration region in front of the orifice is expanded and the recirculation length is shortened with increasing β. In the Q contours, it is shown that with higher β, the strength of the vortical structures reduces and almost disappears with $\beta = 0.75$. From $\beta = 0.25\sim0.5$ in Fig 4.10 (a)~(b), it can be seen that the vortical structures strengthen in the orifice. In Fig. 4.10 (c), the vortical structures tend to be separated into two small eddies, which are located in the two edges of the orifice plates.

Table 4.7 Recirculation length with respect to change in β at $Re = 16$

β	Recirculation length (L/D)
0.25	2.5391
0.5	0.6766
0.75	0.1410

a)

b)

c)
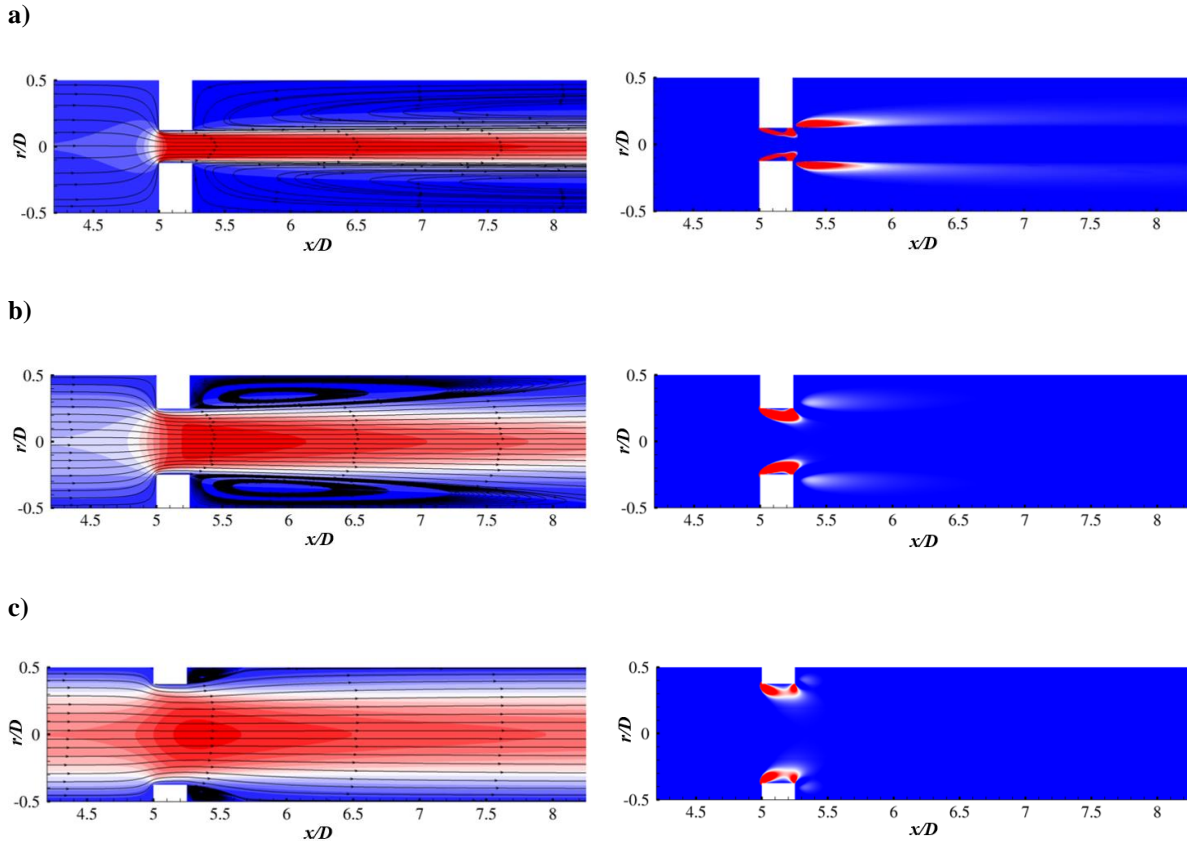
Figure 4.10 Streamwise velocity contours, streamlines and Q-criterion contours at $Re = 100$ for (a) Case 5, (b) Case 2 and (c) Case 6.

4.4.5 Effect of t on flow characteristics

In Fig. 4.11, the dependencies of streamwise velocity contours, streamlines and Q criterion contours on t are shown. It can be observed that there is negligible change in the streamwise velocity contours with varying t. It can also be seen that increasing the thickness does not seem to alter the recirculation length significantly, which is also observed in the results in Sahin & Ceyhan (1996). The vortical structures after the orifice becomes slightly weaker with larger t. With $t = 0.125$ and $t = 0.25$, there is only one vortical structure formed inside the orifice. With $t = 0.5$, the vortical structure starts separating and with $t = 1, 2$ the vortical structure is

formed into two regions in the upstream and downstream, located at the inlet and edge of the orifice and the two vortical structures are weakly interacted.

a)

b)

c)

d)

e)
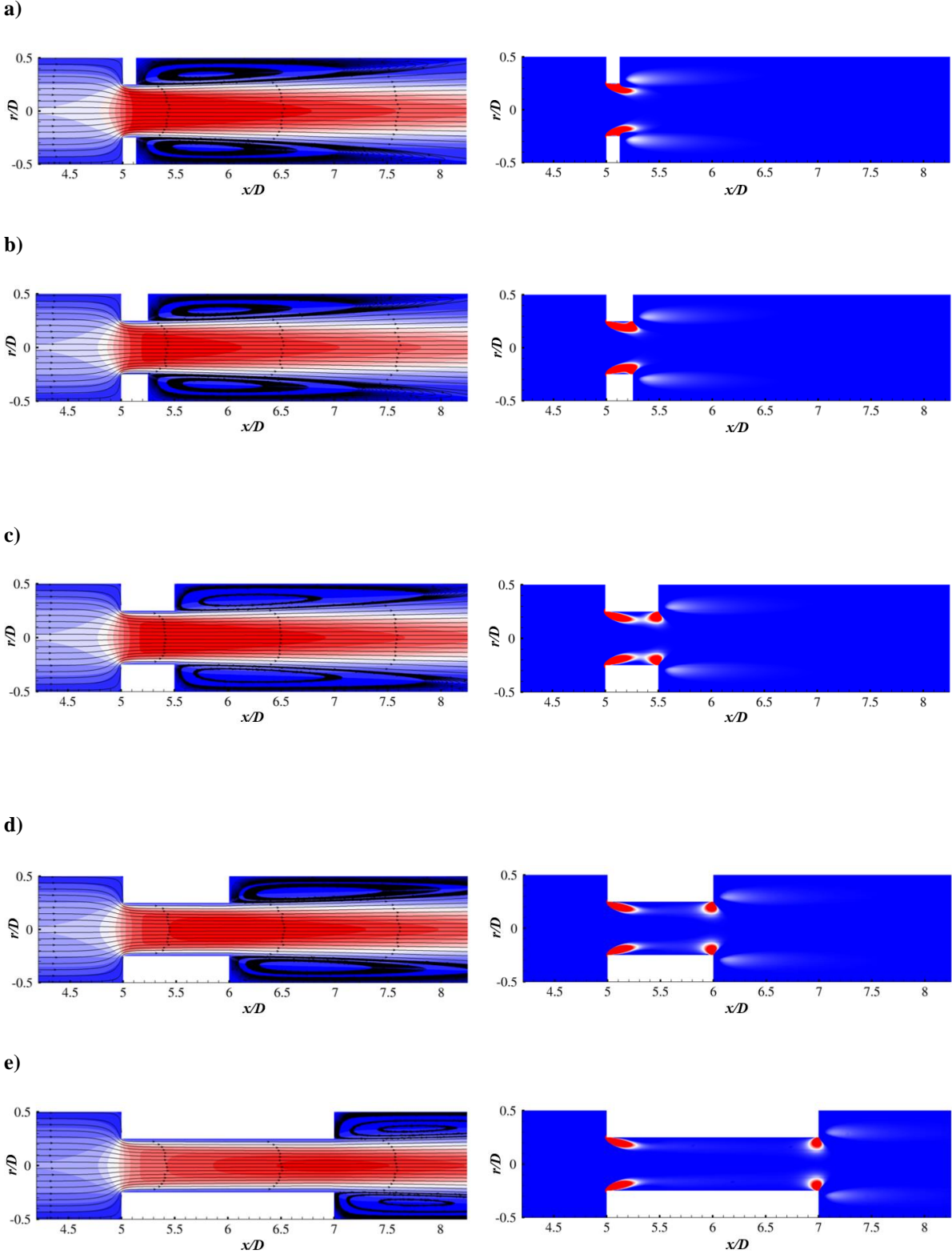
Figure 4.11 Streamwise velocity, streamlines and Q-criterion contours at $Re = 100$ for (a) Case 1, (b) Case 2, (c) Case 3, (d) Case 4 and (e) Case 5.

Chapter 5 Turbulent flow through a square edged orifice inside a pipe

The present chapter outlines the convergence studies, validation studies and present results of the numerical investigation of turbulent flow through a square edged orifice. Firstly, the computational domain and boundary conditions are described, and a validation study of the inlet conditions and control parameters are presented. Secondly, the results are validated by comparing the present calculated discharge coefficient with previous published experimental and numerical results. The effects of Re, t and β on the flow are discussed by presenting the streamwise velocity contours, streamline and Q-criterion contours.

5.1 Turbulent inlet conditions

Pre-processing is done by generating the turbulent inlet conditions and defining the control parameters. To ensure that the flow passing through the orifice is fully developed turbulence, a convergence and validation study of a long straight pipe are performed. The profiles of the flow variables from the fully developed turbulence from the numerical results of the straight pipe are further extracted and implemented as inlet conditions for the numerical investigation of turbulent flow through a square-edged orifice inside a pipe.

5.1.1 Inlet conditions for turbulent flow in a straight pipe

The straight pipe has a diameter of $D = 1m$ and length of $L = 50D$. Computational domain is shown in Fig. 5.1.
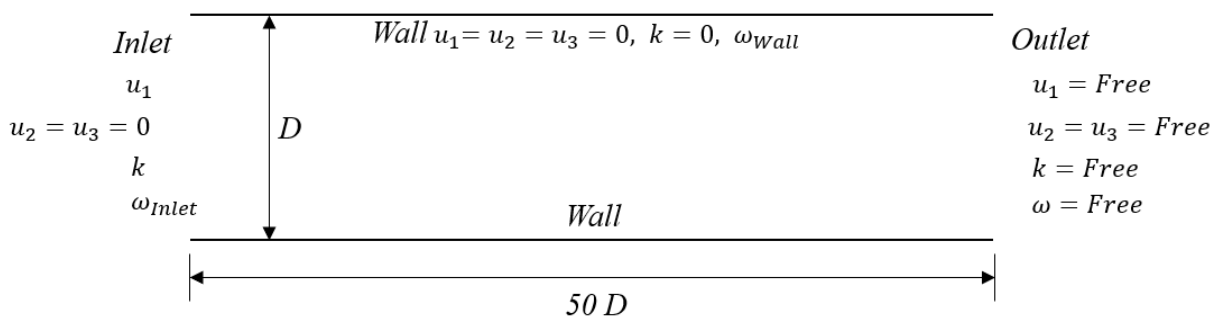
Figure 5.1 Computational domain for straight pipe without orifice

The boundary conditions are set as follows:

Inlet: At the inlet, the velocity is set to be uniform as $u_1 = 1 \; m/s, u_2 = 0, u_3 = 0$ and the pressure is set to be zero normal gradient. The turbulent kinetic energy k and the specific dissipation rate ω is set to be a fixed value, estimated from Eq. (5.1) and Eq. (5.2).

$$k = \frac{3}{2}(u_{avg} \cdot I)^2 \tag{5.1}$$

$$\omega_{inlet} = \frac{\sqrt{k}}{l} \tag{5.2}$$

where $u_{avg} = 1 \; m/s$ is the average velocity at the inlet, $I = 0.16 Re^{-1/8}$ is the turbulent intensity and $l = D$ is the hydraulic diameter of the pipe.

Wall: Velocity is set to a fixed value of $u_1 = u_2 = u_3 = 0$ (No-slip boundary condition), and the pressure is set to be zero normal gradient. The turbulent kinetic energy k is set to be a fixed value $k = 0$, and the specific dissipation rate ω at the walls is defined as a wall function with an initial value estimated from Eq. (5.3).

$$\omega_{wall} = 10 \cdot \frac{6\nu}{\beta_1 (\Delta y_1)^2} \tag{5.3}$$

where ν is the kinematic viscosity of the fluid, $\beta_1 = 0.075$ is an experimental constant, and Δy_1 is the distance from the wall to the closest grid cell to the wall. Δy_1 is estimated from rearranging Eq. (2.21) as:

$$\Delta y_1 = \frac{y^+ \cdot \nu}{u^*} \tag{5.4}$$

where y^+ is set to be equal 1, and u^*(Eq (2.18)) can be approximated as:

$$u^* = \sqrt{\frac{1}{2} C_f U^2} \tag{5.5}$$

where $C_f = 0.079 \cdot Re^{-0.25}$.

Outlet: At the outlet, the velocity u_1, u_2, u_3 is set to zero normal gradient, and the pressure is set to be a fixed value of $p = 0$. The turbulent kinetic energy k and the specific dissipation rate ω are set to be zero normal gradient.

5.1.2 Convergence and validation studies on straight pipe

Four different grid resolutions of the long straight pipe are used in present convergence study and validated by comparing the semi-logarithmic relation between y^+ and u^+ obtained from experimental results by Toonder & Nieuwstadt (1997), at Re = 10 000. The different grid resolutions are shown in Table 5.1 and Fig. 5.2 shows the resulting streamwise velocity from the convergence and validation study.
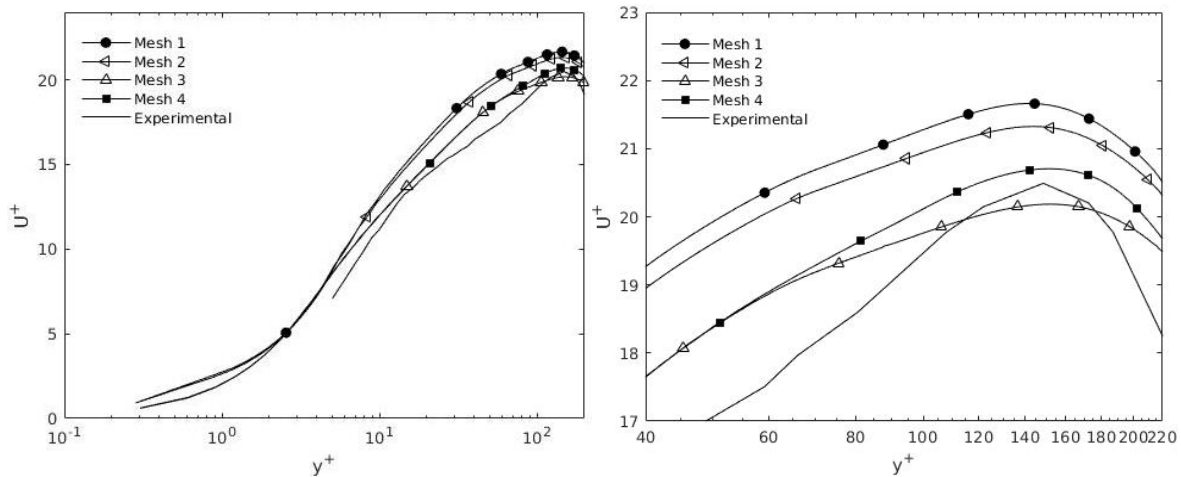
Figure 5.2 Convergence and validation study of the straight pipe for four different grid resolutions, compared with previous experimental results (Toonder & Nieuwstadt, 1997).

Table 5.1 Grid resolution of the different meshes

Mesh	Grid resolution	Mean deviance from experimental results
Mesh 1	1 655 500	14.74%
Mesh 2	2 003 760	14.33%
Mesh 3	2 528 800	10.53%
Mesh 4	3 447 280	10.9%

It is shown from Fig. 5.1 that the resulting streamwise velocity of Mesh 3 and Mesh 4 shows small discrepancy only in the center of the pipe. Mesh 4 produce a more similar trend than Mesh 3 compared with the experimental results, and is therefore chosen for further study.

5.2 Computational domain and boundary conditions

The computational domain setup is in the same manner as defined in Section 4. The orifice is inserted at $L/2$ inside a pipe with diameter of $D = 1$m, and the pipe length is set to be $L = 10D$ without the additional length of the orifice. Twelve different cases are simulated at different Reynolds number (defined by the inlet flow rate velocity and the diameter of the pipe), where the ratios of the orifice thickness to pipe diameter ratio are $t = 0.125, 0.25, 0.5, 1, 2$ and the orifice diameter to pipe diameter ratio are $\beta = 0.25, 0.5, 0.6$. The Reynolds numbers in this study are $Re = 2500, 4900, 10000$ and 40000. Fig. 5.3 gives an outline of the computational domain and the boundary conditions.
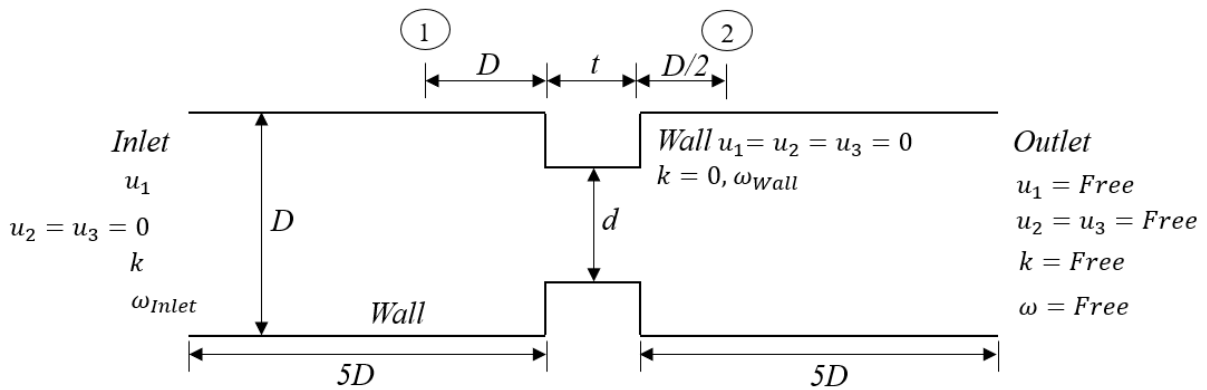
Figure 5.3 Computational domain for straight pipe with orifice

The boundary conditions for the turbulent flow are set as follows:

Inlet: At the inlet, the velocity u_1 is set to be fixed values obtained from the turbulent flow in straight pipe, $u_2 = u_3 = 0$, and the pressure to be zero normal gradient. The turbulent kinetic energy k and specific dissipation rate ω is set to be fixed values obtained from the turbulent flow in straight pipe.

Wall: At the walls, the velocity is set to a fixed value of $u_1 = u_2 = u_3 = 0$ (no-slip boundary condition), and pressure to be zero normal gradient. The turbulent kinetic energy k is set to a fixed value of $k = 0$ and the specific dissipation rate ω at the walls is defined as a wall function with an initial value estimated from Eq. (5.3).

Outlet: At the outlet, the velocity is set to be zero normal gradient, and the pressure to be a fixed value of zero. The turbulent kinetic energy k and specific dissipation rate ω are set to be zero normal gradient.

5.3 Convergence study

A grid convergence study has been performed for four different mesh grid resolutions, with orifice thickness to pipe diameter ratio $t = 0.5$ and orifice diameter to pipe diameter $\beta = 0.5,$ at $Re = 10000$. Two quantities are checked for the grid convergence, velocity and pressure through the orifice and the streamwise velocity profiles in front of and behind the orifice. The measurement locations are shown in Fig. 5.3. The computational grids in the axis and cross section directions of the present study are shown in Fig. 5.4. The grids in the axis direction are refined around the orifice region. The first cell layer height near the wall Δy_1 is estimated from Eq. (5.4) to be $y^+ \sim 1$. Fig. 5.5 shows the pressure and streamwise velocity distributions along the streamwise direction through the orifice for the different mesh resolutions and Fig. 5.6 shows the velocity profile before and after the orifice plate. Table 5.2 shows the different grid numbers and their corresponding discharge coefficients C_d, as well as the deviance in pressure distribution through orifice compared with that of the finest mesh.

Table 5.2 Result of the cases with different grid resolutions, with the maximum Courant number, $Co_{max} = 0.8$

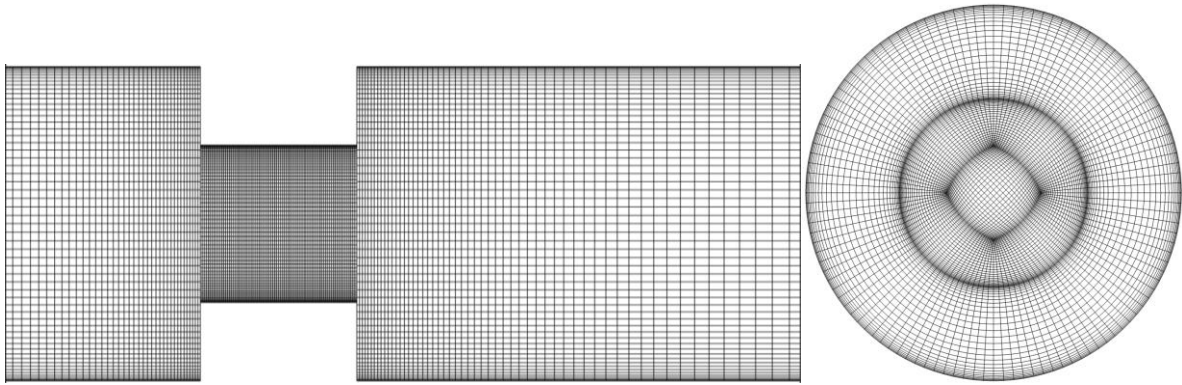| Case	Elements	C_d	Mean deviance pressure distribution from Mesh 4
Mesh 1	1 683 680	0.7704 (0.85%)	0.964%
Mesh 2	2 314 310	0.7717 (0.68%)	0.712%
Mesh 3	3 229 044	0.7763 (0.09%)	0.149%
Mesh 4	4 213 484	0.7770 (-)	-

Figure 5.4 Example of Mesh 1, β = 0.5 and t=0.5, around orifice region and grid inside pipe
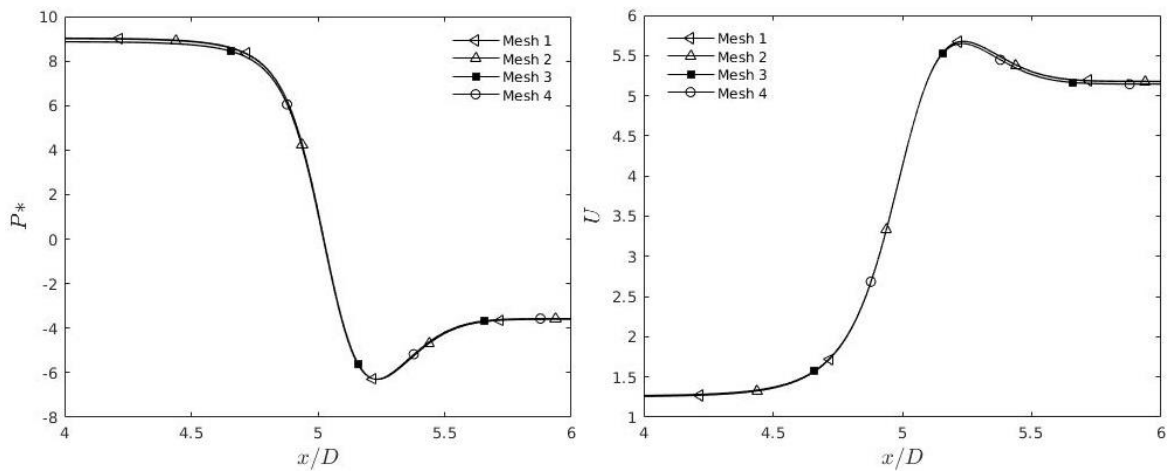

Figure 5.5 Distribution of pressure and streamwise velocity along the streamwise direction through the orifice plate
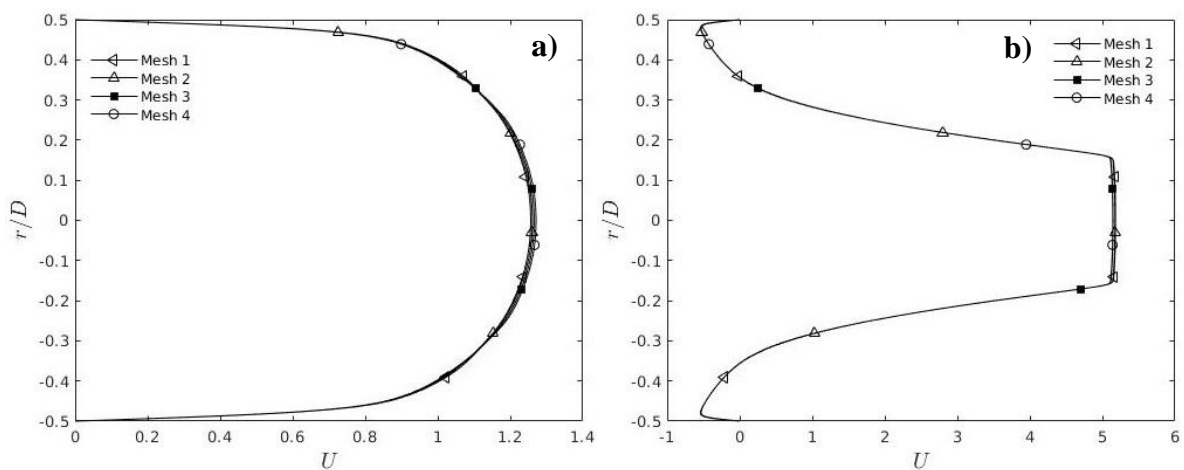

Figure 5.6 Streamwise velocity profile inside pipe for a) in front of orifice and b) behind orifice

The adjustable time-step with a maximum allowable Courant number of 0.8 gives a timestep interval in the range $0.00028 \leq \Delta t_{avg} \leq 0.00044$. From the numerical results, the average Courant number have been kept low for all grid resolutions in the range $0.0127 \leq Co_{avg} \leq 0.0148$. Courant number are observed to reach the maximum allowable in the cross-sectional area between the pipe and the orifice plate, due to the flow area is restricted and the flow is accelerated.

As seen from Fig. 5.5 and Table 5.2, all mesh resolutions have been converged and the mean deviance in the pressure distribution for all resolutions are less than 1% from the finest mesh. The velocity profiles show negligible difference along the radial direction for all four mesh resolutions, as shown in Fig.5.6. Taking the computational cost into consideration, the grid resolution of Mesh 1 is used in the further study.

5.4 Results and discussion

In this section, the results obtained from the numerical simulations of the turbulent flow through a straight pipe with a square edged orifice plate are presented. In section 5.4.1, calculated discharge coefficient for cases with different t and constant β are obtained and compared against the previous experimental and numerical studies. In section 5.4.2, the resulting discharge coefficients for the different orifice characteristics are presented and discussed. In section 5.4.3, 5.4.4 and 5.4.5, the effects of Re, β and t on the flow characteristics are discussed by presenting the streamwise velocity contours, streamlines and Q-criterion contours.

5.4.1 Validation study

To ensure the accuracy of the present simulations, a validation study is carried out by investigating the discharge coefficients (Eq. (2.30)) achieved with an orifice with a fixed $\beta = 0.6$ and a range of $t = 0.08$ (1/12), 0.25, 0.5, 1. This is further compared with the previous published experimental results by Johansen (1930) and the numerical results by Tunay et al (2004). Tunay used the standard $k - \varepsilon$ turbulence model and power law velocity profile (Eq. (5.5)) at the inlet.

49

In the present validation study, the same boundary conditions as in the turbulent straight pipe in section 5.1 are used. However, in order to compare with the previous results in Tunay et al (2004), a turbulent velocity profile obtained from Eq. (5.5) is implemented at the inlet.

$$u(r) = u_{max} \left(1 - \frac{r}{R}\right)^{1/n} \tag{5.5}$$

where u_{max} is set to be 2 *m/s,* exponent n is set to be 7, the same values as that in Tunay et al (2004).

The results from the present study compared with the previous published data are shown in Fig. 5.7. The different cases in the study are presented in Table 5.3. For $t = 1/12$, the present results are slightly overestimated for all Reynolds numbers with an average error of 8.69% compared with the experimental results from Johansen (1930) and numerical results from Tunay et al. (2004). In general, the present results are in good agreement with previous numerical results for $t \geq 0.25$. For $t = 1$, the results are slightly overestimated at $Re = 2\ 500,\ 4\ 900$ but is approximately accurate at the higher Re. For smaller $t,$ there is overestimations at the four Re with an average error of 2.75% from the previous numerical results by Tunay et al (2004). As a result, the present model is validated against the previous data.

Table 5.3 Overview of the different cases in the validation study of straight pipe with an orifice

Case	β	t	Cells
1	0.6	1/12	1 683 682
2	0.6	0.25	1 683 682
3	0.6	0.5	1 683 682
4	0.6	1	2 020 082
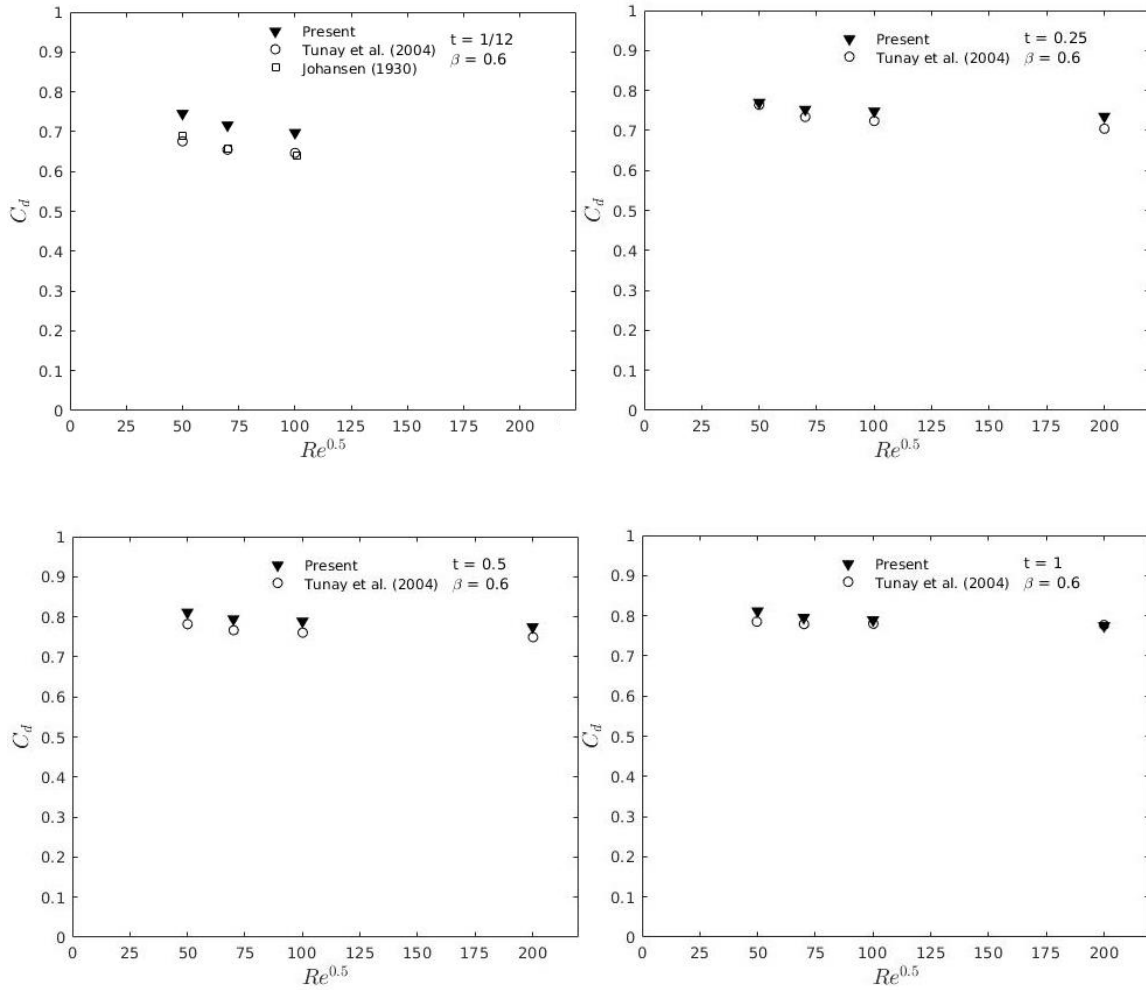
Figure 5.7 Variation of discharge coefficients with increasing Re, compared with results from Johansen (1930) and Tunay et al (2004)

5.4.2 Discharge coefficient

Discharge coefficients for different orifice characteristics at different Re are presented in Fig. 5.8. For high Re, it can be observed that the variation of discharge coefficients varies much less than for the low Re presented in section 4.4.2. In addition to the lower variation, the discharge coefficients are also decreasing with increasing Re. For all orifice characteristics, it can be observed a descending of the discharge coefficient between $Re = 2\,500$ and $Re = 4\,900$, and the discharge coefficient starts stabilizing from $Re = 10\,000$.

Table 5.4 Overview of simulation cases in present study

Case	β	t	Cells
5	0.25	0.25	2 314 312
6	0.5	0.25	1 683 682
7	0.5	0.125	1 683 682
8	0.5	0.5	1 683 682
9	0.5	1	2 356 482
10	0.5	2	2 356 482
11	0.6	1/12	1 683 682
12	0.6	0.25	1 683 682
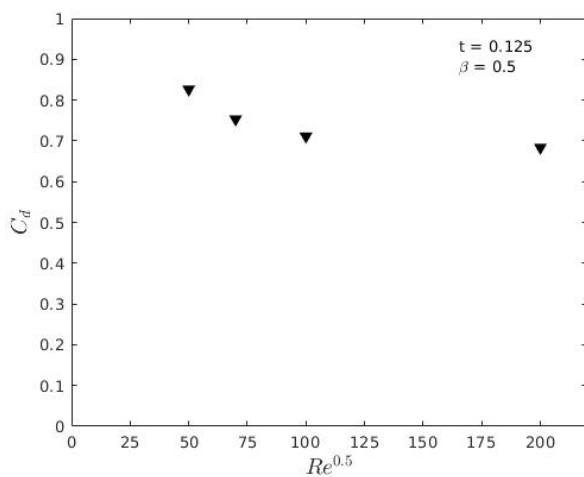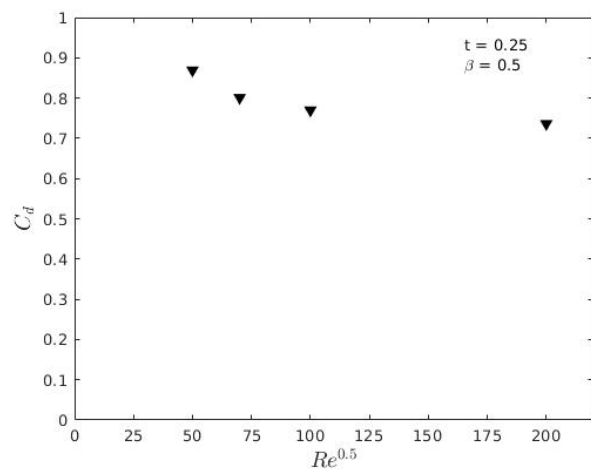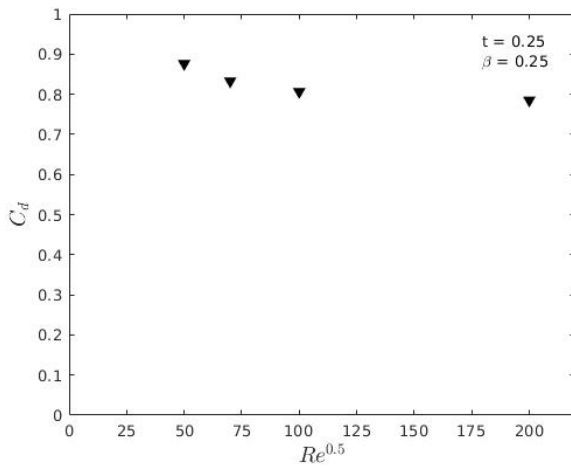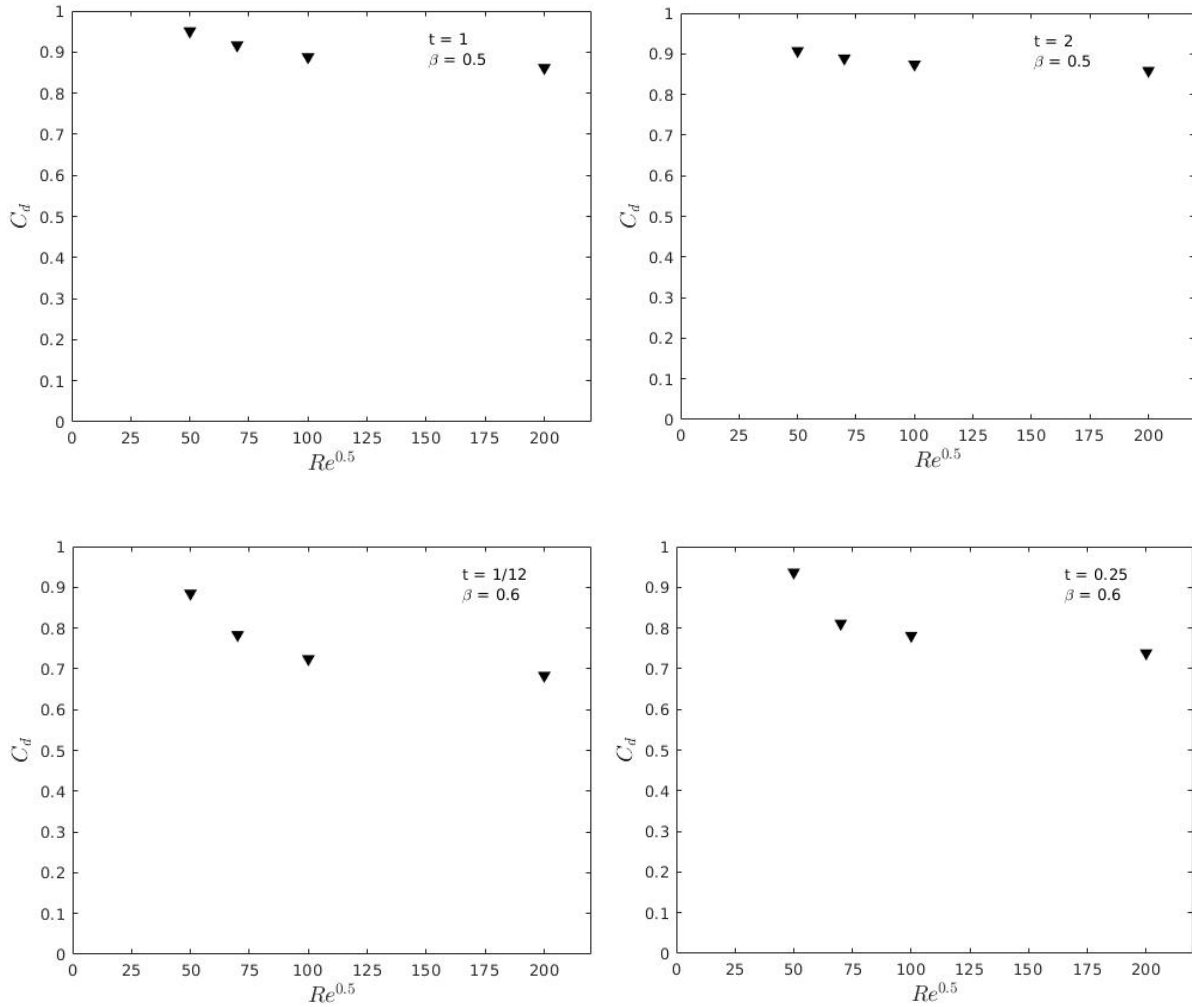
Figure 5.8 Variation of discharge coefficient with increasing Reynolds number
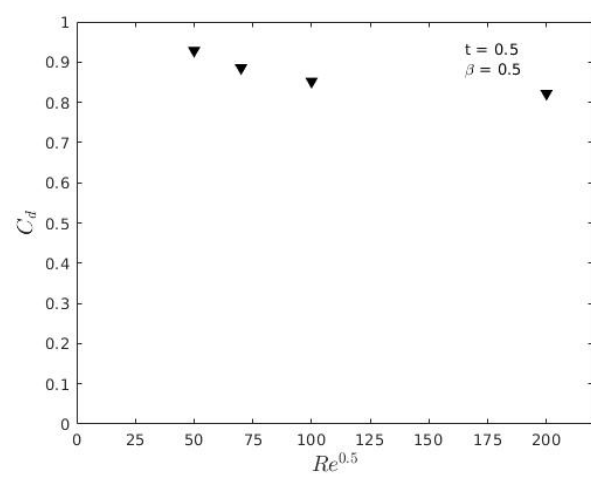
5.4.3 Effect of Reynolds number on flow characteristics

The effects of Re on the flow fields of interest are studied in terms of the streamwise velocity contours, the streamlines and the Q-criterion contours in Fig. 5.10. It is observed that with the increasing Re, the jet flow passing the orifice is slightly accelerated. The recirculation motion behind the orifice is slightly suppressed from $Re = 2\,500$ to $Re = 4\,900$, as shown in Fig 5.9. From $Re = 4\,900$ to $Re = 40\,000$, the recirculation length becomes constant. At lower Re, there are small recirculation motion around the corner behind the orifice plate and they tend to be suppressed at increasing Re. The large vortical structures are identified by Q-criterion shown in Eq. (4.1). Behind the orifice plates display irregular shapes compared with that in laminar flow case in Section 4.4.3. The size of the large vortical structure becomes smaller in the cross-section direction while it becomes larger in the streamwise direction. At

higher *Re*, the vortical region around the shear layer behind the orifice plates becomes weaker and small irregular vortices appears around the corner of the orifice plate.
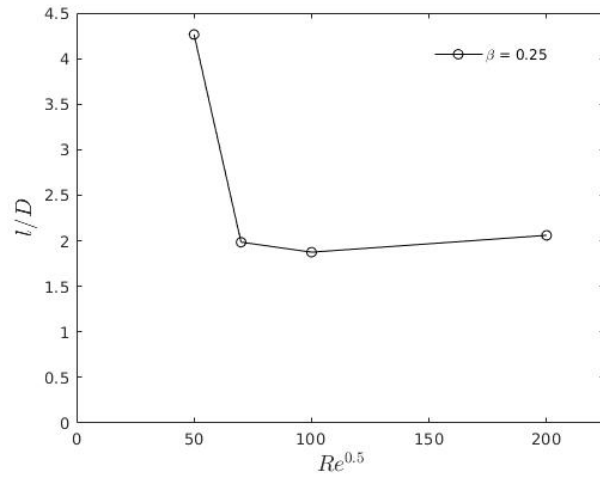
Figure 5.9 Change in recirculation length with increase in *Re* for $\beta = 0.25$ and $t = 0.25$

a)
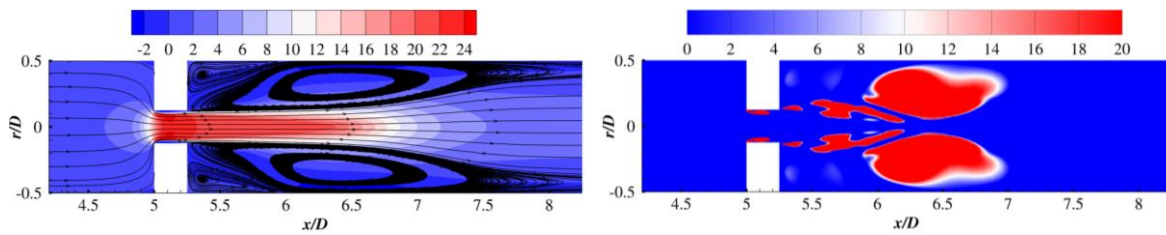
b)
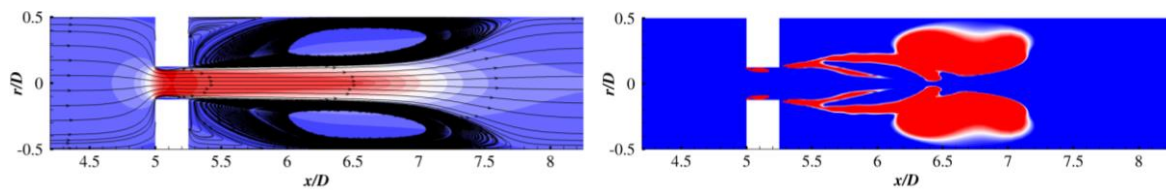
c)
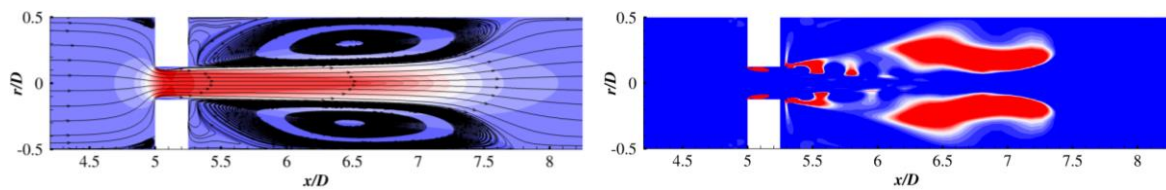
d)
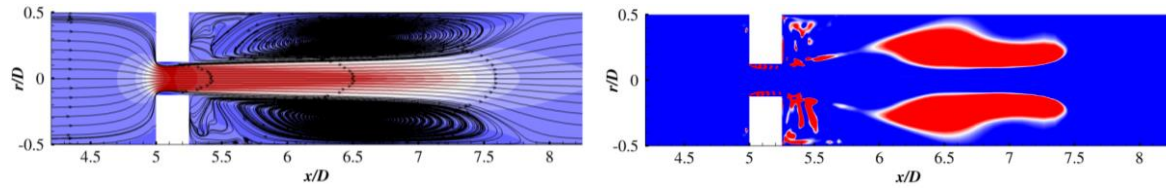
Figure 5.10 Streamwise velocity contours, streamlines and Q-criterion contours for β = 0.25 and $t = 0.25$ at a) $Re = 2500$, b) $Re = 4900$, c) $Re = 10000$ and d) $Re = 40000$

5.4.4 Effect of β on flow characteristics

The effects of β on the flow characteristics are studied at $Re = 40000$ with $t = 0.25$, streamwise velocity contours, the streamlines and the Q-criterion contours are presented in Fig. 5.12. The acceleration region of the flow passing the orifice is expanded with increasing β, and the length of the jet flow is expanded. Variations of the flow recirculation length with Re is shown in Fig. 5.11. The recirculation length is increased from β = *0.25-0.5* and is further reduced with increasing β. Vortical structures in the downstream of the flow is drastically weaken from β = 0.25 – 0.5, and are further slightly reduced with increasing β. Furthermore, the vortical structure inside the orifice is observed to become stronger with increasing β and small vortical regions are formed in the corner of the front face of the orifice plate.
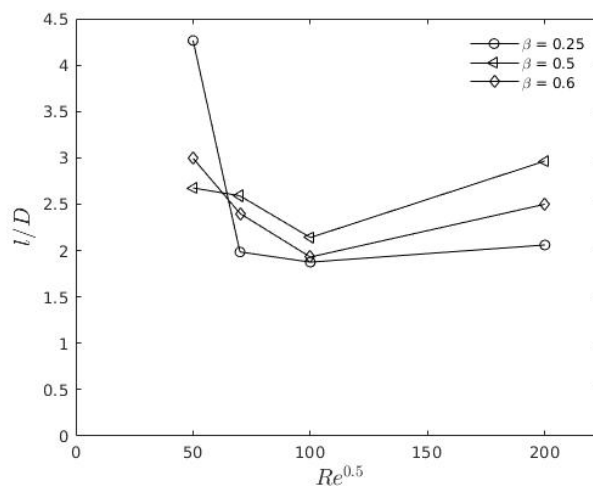
Figure 5.11 Change in recirculation length with increase in Re for different β with $t = 0.25$

a)

b)

c)
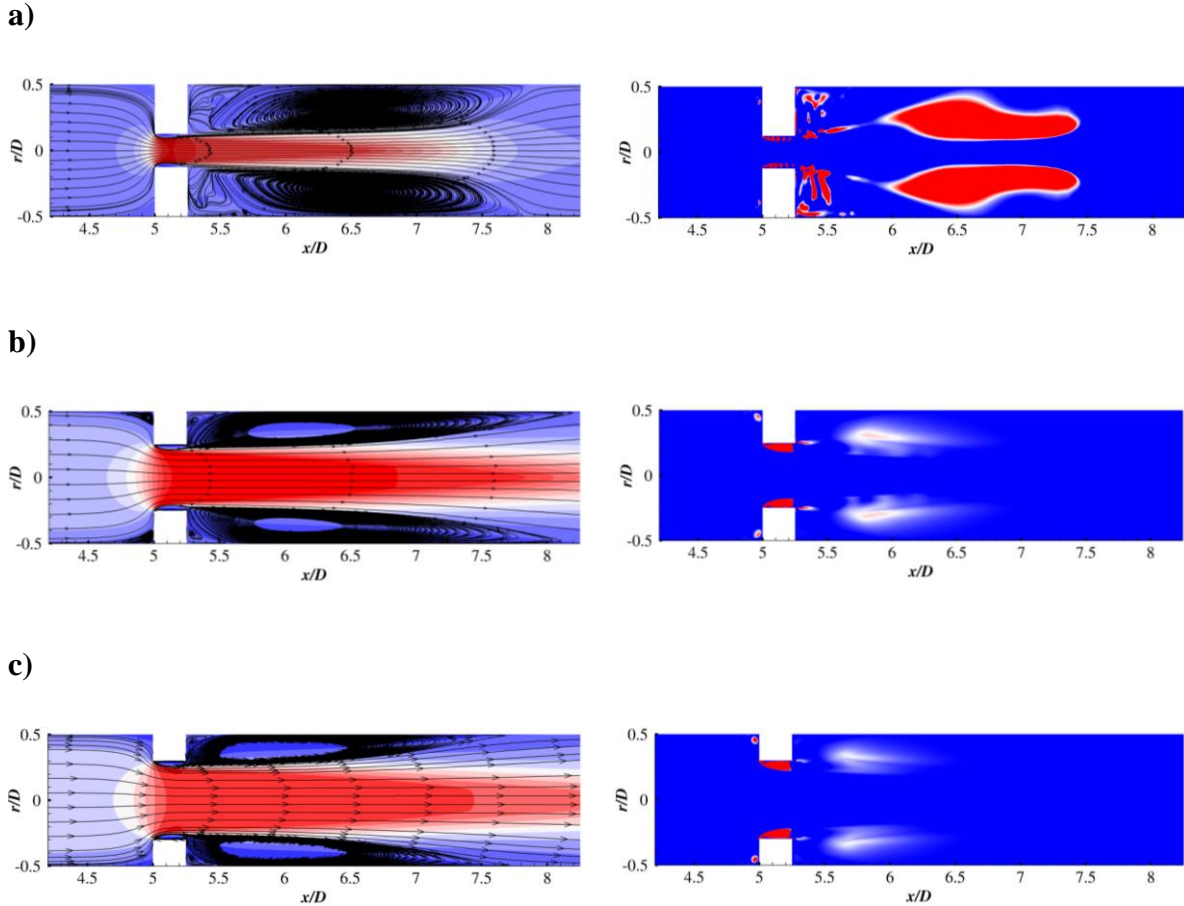
Figure 5.12 Streamwise velocity contours, streamlines and Q-criterion contours for $= t =$ 0.25 at a) $\beta = 0.25$, b) $\beta = 0.5$ and c) $\beta = 0.6$

5.4.5 Effect of t on flow characteristics

Effect of t on the flow characteristics are studied at $Re = 40\,000$ and $\beta = 0.5$ and streamwise velocity contours, the streamlines and the Q-criterion contours are presented in Fig. 5.14. It can be observed that the streamwise acceleration region of the flow through the orifice is weakened in the downstream with increasing t. however, increasing the thickness of the orifice seems to have little effect on the recirculation of the flow in the downstream, as observed in section 4.4.5. the vortical structure bears similarity with the observations in section 4.4.5 for laminar flow. Increasing the thickness t separates the vortical structure inside the orifice into two regions located at the edges of the orifice. With further increasing t, the vortical structure around the leading edge of the orifice seems to be unchanged. However, one noticeable difference with the laminar flow case is that the vortical structure around the back edge of the orifice is suppressed. Strong but thin vorticity regions start to appear around the shear layer behind the orifice plate.
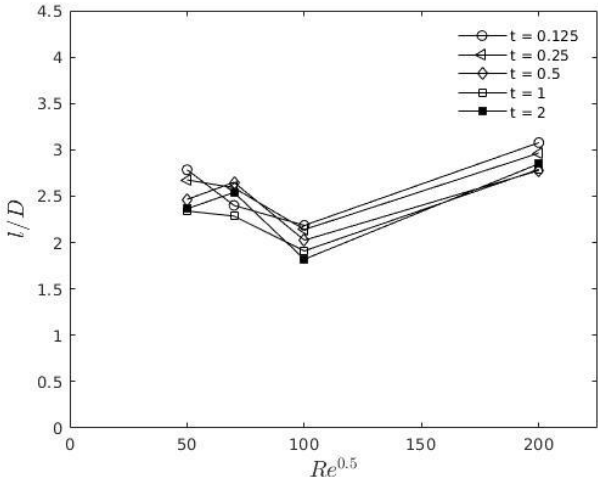
Figure 5.13 Change in recirculation length with increase in Reynolds number for different thicknesses

a)

b)

c)

d)

e)
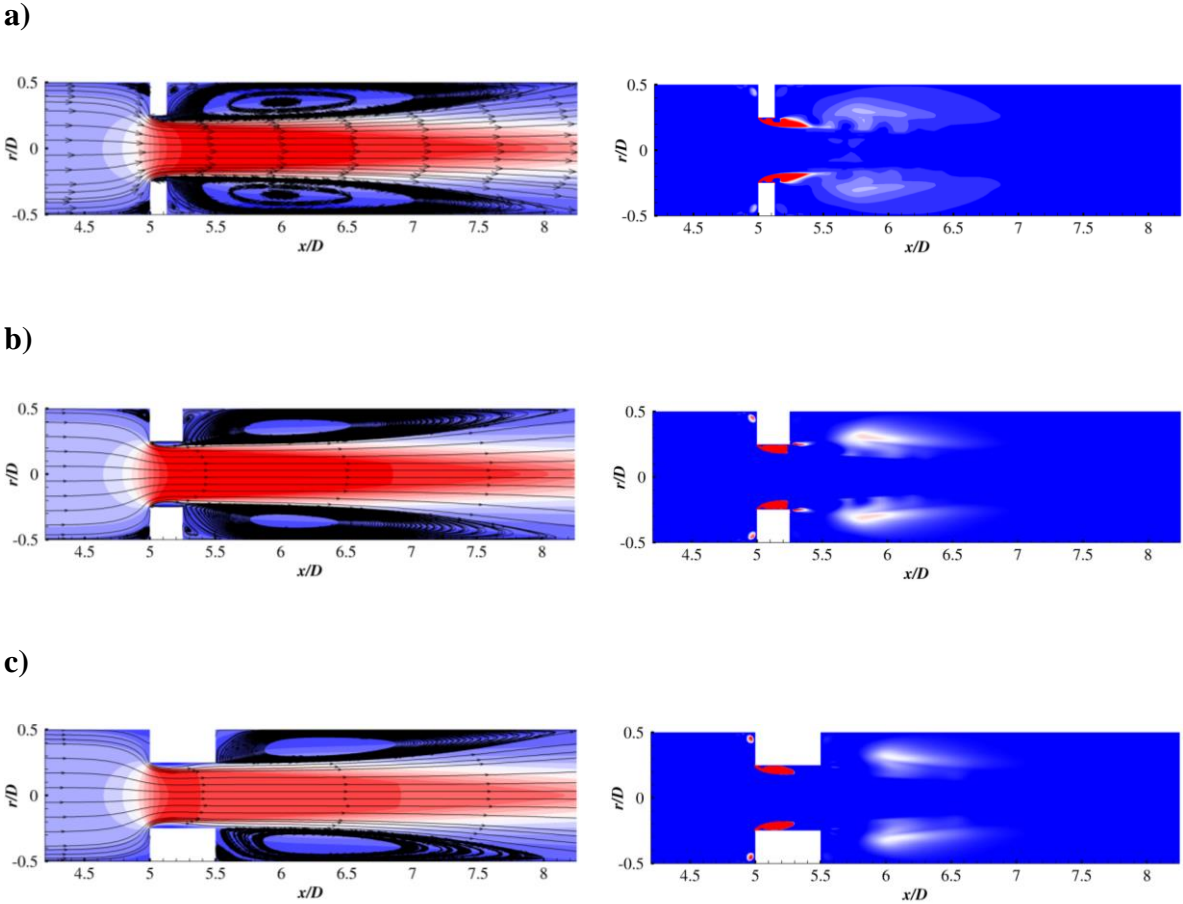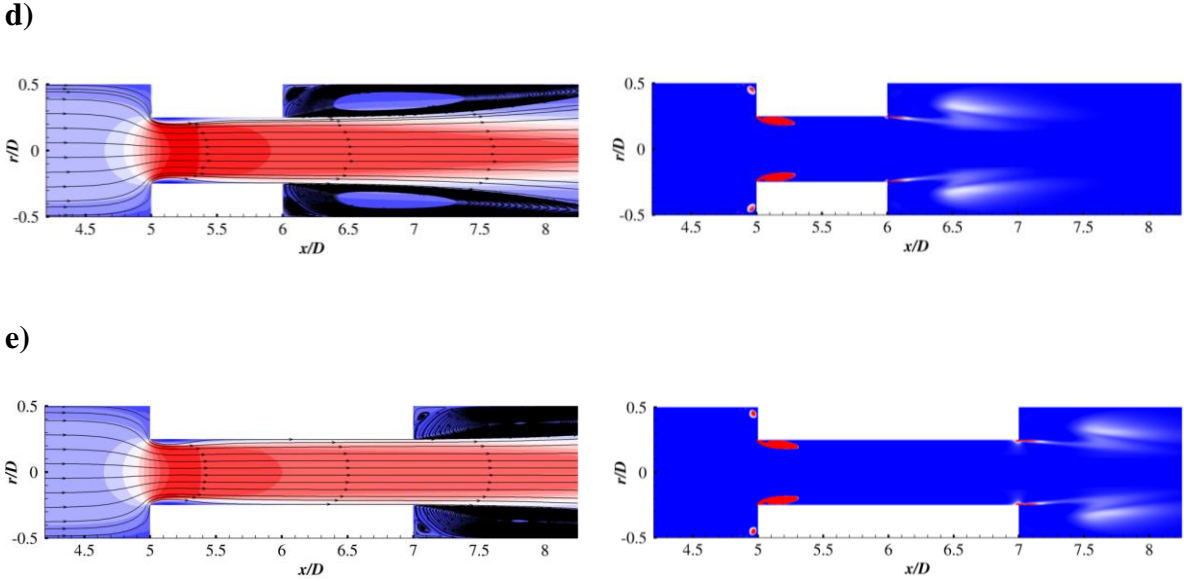
Figure 5.14 Streamwise velocity contours, streamlines and Q-criterion contours for β = 0.5 at a) $t = 0.125$, b) $t = 0.25$, c) $t = 0.5$, d) $t = 1$ and e) $t = 2$

Chapter 6 Conclusion and further work

In this present study, CFD simulations has been carried out to obtain the discharge coefficients for different orifice characteristics and to investigate the flow behavior through the orifices. Numerical studies are conducted in two different flow regimes, laminar flow regime at $0 \leq Re \leq 400$ and turbulent flow regime at $2\ 500 \leq Re \leq 40\ 000$. The present numerical simulations are based on Navier-Stokes equations under the assumptions that the flow is incompressible, viscous, and a $k - \omega$ SST turbulence model has been used for the turbulent flow regime. The main conclusions are as follows:

1. Laminar flow through a square edged orifice inside a pipe.

- The resulting discharge coefficients are in good agreement with the published numerical and experimental data, except that there are underestimations at low Re.

- The flow is accelerated from a distance before the orifice plate and this is more prominent with increasing Re. The jet flow expansion is observed to shrink at higher Re and the length of the jet is increased. The acceleration region is expanded with increasing β and no noticeable change is observed with different orifice thickness t.

- The vortical structure after the orifice is weakened with increasing Re and β. The vortical structure in the orifice separates with increasing t and two vortical structures forms at the two edges of the orifice plates.

- The recirculation length of the flow increases with Re and decreases with increasing β and there is no significant change with increasing t. The flow re-attaches to the pipe wall quickly at low Re with small β. However, at higher Re with lower β the recirculation length cannot be predicted as the re-attachment occurs outside the computational domain.

59

2. Turbulent flow through a square edged orifice inside a pipe.

- The resulting discharge coefficients are in satisfying agreement with the previous published numerical and experimental results. For $t = 1/12$, the present results are slightly overestimated for all Re with an average error of 8.69% from the published data. For $t \geq 1/12$, smaller overestimations are observed, but not consistent for a specific Re and with a maximum error of 2.75%.

- The jet flow out of the orifice increases slightly with increasing Re. The acceleration region of the flow passing the orifice is expanded with increasing β, and the length of the jet flow is expanded. The streamwise acceleration region of the flow through the orifice is weakened in the downstream with increasing t

- The size of the vortical structure becomes smaller in the cross-section direction while it becomes larger in the streamwise direction with increase in Re. At higher Re, the vortical region around the shear layer behind the orifice plates becomes weaker and small irregular vortices appears around the corner of the orifice plate. Vortical structures in the downstream of the flow are drastically weaken from $\beta = 0.25 - 0.5$, and are further slightly reduced with increasing β. Vortical structures inside the orifice are observed to become stronger with increasing β and small vortical regions are formed around the corner of the front face of the orifice plate. The vortical structure bears similarity with the observations for laminar flow. Increasing the thickness t separates the vortical structure inside the orifice into two regions located at the edges of the orifice. With further increasing t, the vortical structure around the leading edge of the orifice seems to be unchanged.

- Reduction of the recirculation length is observed from $Re = 2500$ to $Re = 4900$, and starts to stabilize slightly with further increase in Re. Recirculation length is increased from $\beta = 0.25$-0.5 and is further reduced with increasing β. Increasing the thickness of the orifice can be shown to have little effect on the recirculation of the flow in the downstream region.

6.1 Recommendations for further work

Below are some suggested ideas for further future work:

- Study on the potential structural vibration caused by the flow through the orifice for different orifice characteristics and at a variety of Reynolds numbers.

- Study on the multiphase flow through an orifice. Investigate the behavior of the flow through the orifice and compare with single phase flow.

- Study on the flow through multi-hole orifices, venturi and nozzle shaped flowmeters. Compare different obstruction shapes and determine the suitable areas for application of the different obstruction flow meters.

References

Anantharaman V., Waterson N., Nakiboglu G., Persin M. & van Oudheusden B. 2016. Experimental investigation of turbulent flow through single-hole orifice placed in a pipe by means of time-resolved Particle Image Velocimetry and unsteady pressure measurements. In FIV: Proceedings of the 11th International Conference on Flow-Induced Vibrations: The Hague, The Netherlands.

Çengel Y. & Cimbala J. 2017. Fluid Mechanics Fundamentals and Applications. 4th ed. Singapore: Mc Graw Hill Education.

Cottrell M. 2006. Flow measurement. Missouri University of Science and Technology.

Den Toonder J.M.J. & Nieuwstadt F.T.M. 1997. Reynolds number effects in a turbulent pipe flow for low to moderate Re. Physics of fluid 9. DOI: 10.1063/1.869451.

Dickerson P. & Rice W. 1969. An investigation of very small diameter laminar flow orifices, Transactions of the ASME, 546-548.

Ding T.M. & Wang Y. 2015. Comparison research on hydraulic characteristics of three types of orifice plate, The open fuels & energy science journal, 43-46.

Eiamsa-ard S., Ridluan A., Somravysin P. & Promvonge P. 2008. Numerical investigation of turbulent flow through circular orifice, KMITL scientific journal Vol.8, 43-50.

Gao J. & Wu F. 2019. Investigation of flow through the two-stage orifice, Engineering Applications of Computational Fluid Mechanics, 13:1, 117-127, DOI: 10.1080/19942060.2018.1561517.

Hollingshead C.L., Johnson M.C., Barfuss S.L. & Spall R.E. 2011. Discharge coefficient performance of Venturi, standard concentric orifice plate, V-cone and wedge flow meters at low Reynolds numbers, Journal of Petroleum Science and Engineering, 559-566.

Holzmann T. 2017. Mathematics, Numerics, Derivations and OpenFOAM(R), Holzmann CFD, Leoben, fourth edition.

Hornbeck R.W. 1964. Laminar flow in the entrance region of a pipe. Appl. sci. Res 13: 224. https://doi.org/10.1007/BF00382049

Hunt J. C. R., Wray A. & Moin, P. 1988. Eddies, stream, and convergence zones in turbulent flows. Center for Turbulence Research Report CTR-S88.

Jasak H. 1996. Error Analysis and Estimation for the Finite Volume Method with Applications to Fluid Flows. Phd thesis, Imperial College.

Kundu P.K. & Cohen I.M. 2008. Fluid Mechanics, 4th edition, Elsevier inc.

Lakshmana Rao N.S. & Sridharan K. 1971. Loss characteristics of long orifices, Fourth Australian conference on hydraulics and fluid mechanics, 246-251.

Launder B.E. & Spalding D.B. 1972. Mathematical models of turbulence, Academic Press, London.

Menon E.S. 2015. in Transmission Pipeline Calculations and Simulations Manual.

Menter F. 1994. Two-equation eddy-viscosity turbulence models for engineering applications. AIAA Journal 32, 1598 – 1605.

Miller R. P. & Nemecek I. V. 1958. Coefficients of discharge of short pipe orifices for incompressible flow at Reynolds numbers less than one. ASME paper number 58-A-106, presented at the ASME annual meeting, New York.

Miller R. W. 1997. Flow Measurement Engineering Handbook, 3rd ed. New York: McGraw-Hill.

Mittal R.C. & Sharma P.K. 1987. Numerical solution of a viscous incompressible flow problem through an orifice, Applied Scientific Research 44, 361-375.

Moukalled F., Mangani L. & Darwish M. 2015. The Finite Volume Method in Computational Fluid Dynamics: An Advanced Introduction with OpenFOAM® and Matlab. Springer.

Sahin B. & Ceyhan H. 1996. Numerical and experimental analysis of laminar flow through square-edged Orifice with variable thickness, Transactions of the Institute of Measurement and Control, Vol 18(4), 166-174.

Tunay T., Sahin B. & Akilli H. 2004. Investigation of Laminar and Turbulent flow through an orifice plate inserted in a pipe, Transactions of the CSME/de la SCGM, Vol 28. No.2B 403-414.

Wendt J.F. 2009. Computational Fluid Dynamics: An Introduction. Springer – Verlag Berlin Heidelberg.

Wilcox D.C. 1988. Re-assessment of the scale-determining equation for advanced turbulence models, AIAA Journal, vol. 26, no. 11, pp. 1299-1310.

Appendix

Paper 1: Numerical investigation of laminar flow through an orifice with different thicknesses and heights

Appendix A contains the paper draft which will be submitted to the Journal of Fluids and Structures.

Numerical investigation of laminar flow through an orifice with different thicknesses and heights

Bjørnar Nitter[a], Guang Yin[a], Muk Chen Ong[a]

[a] Department of Mechanical and Structural Engineering and Materials Science, University of Stavanger, 4036, Stavanger, Norway

Abstract: The objective of this paper is to investigate the flow through a circular square edged orifice inside a pipe with various thicknesses and heights. The orifice thickness to pipe diameter ratio varies between $1/8 \leq t \leq 2$, the orifice height to pipe diameter varies between $1/4 \leq \beta \leq 3/4$ and the Reynolds number ranges $0 \leq Re \leq 400$. The present numerical simulations are based on the Navier-Stokes equations under the assumptions that the flow is incompressible, viscous and laminar. The discharge coefficients for the different characteristics of the orifice flowmeter are determined. The validity of the simulations is investigated by comparing present results with previous published numerical and experimental results. The discharge coefficients are in satisfying agreement with previous published numerical and experimental data. Flow fields and vortices in the orifice are analyzed and the effects of Reynolds number on the flow characteristics are also discussed.

1. Introduction

In large processing facilities, the flow rate needs to be measured accurately to achieve an optimal economic operation. There are several ways to measure the flow rate in processing systems. One of the most widely used flow rate meter is the orifice flowmeter. The flow in the pipe is contracted by the sudden change of the cross-section area created by the orifice plates. The flow is then accelerated because of the mass conservation, which causes a static pressure drop due to the energy conservation. The pressure difference measured by the pressure tapping in the upstream and downstream of the flow is combined with Bernoulli equation to obtain the flow rate. A large amount of researches have been carried out to study the flow characteristics inside a orifice flowmeter both by numerical simulations and experiments. One of the first numerical studies on orifice flowmeters was done by Dickerson & Rice (1969) with orifice thickness to pipe length ratio L/D of 1 to 4 at Reynolds number ranging from 27 to 7000, ($Re = UD/\nu$, where U is average velocity of inlet flow, D is the pipe diameter and ν is the kinematic viscosity). They followed the Langhaar entrance flow solution with $\beta < 0.1$ (defined as the ratio of the orifice diameter d to the pipe diameter D: $\beta = d/D$) and obtained good agreement with experimental results for the discharge coefficient (Miller & Nemecek 1958). Lakshmana & Sridharan (1971) presented a theoretical solution to determine the discharge coefficient based on Hornbeck's flow entrance model (Hornbeck 1964), which is used to predict the discharge coefficient for laminar flow in long orifices with small β. Lakshmana & Sridharan (1971) compared the theoretical solution with experimental data and found that the solution is valid with the orifice thickness to pipe diameter ratio $t > 2$ and at an orifice Reynolds number $Re_o < 300$ ($Re_o = U_o d/\nu$, where U_o is average velocity inside the orifice, and d is the orifice diameter). Sahin & Ceyhan (1996) investigated the effects of the orifice plate thickness and Reynolds number by carrying out experiments and numerical simulations. The experimental set up consisted of a hydraulic circuit with the pipe diameter of 13.7mm, a gear pump and a by-pass valve for regulating the flow rate. The pipe length was set to be $170D$ and the orifice diameter and length were set to be $D/2$. The pressure distribution was monitored by an inclined multitube manometer. The numerical solutions based on the steady Navier-Stokes equations was obtained by finite difference method at Reynolds number range of $0 \leq Re \leq 150$ with the orifice thickness range of $1/16 \leq t \leq 1$ and constant β=0.5. Sahin & Ceyhan (1996) obtained a good match between the numerical and experimental results and the streamlines and vorticity contours showed that there are two eddies in the upstream and downstream of the orifice plate. Hollingshead et al. (2011) carried out numerical simulations to obtain the discharge coefficient in four different orifice flowmeters: standard concentric-, venturi-, V-cone- and wedge orifice based on laminar flow conditions at $Re < 2300$ and turbulent flow conditions at $Re \geq 2300$ using Reynolds Average Navier-Stokes

equations combined with a $k - \varepsilon$ model. They discovered that at low Reynolds number, the discharge coefficient decreased rapidly with decreasing Re for Venturi, V-cone and wedge flowmeters. The standard concentric orifice plate meter did not follow the general trends of the other flow meters. Instead as Reynolds number decreased, the discharge coefficient increased to a maximum value before aggressively dropping off with further decrease in the Reynolds number. Gao & Wu (2019) investigated the difference in the transitional flow characteristics of mineral oil through a single and a two staged orifice using experimental and numerical studies. The experimental study was done on a test bench, consisting the orifice, and the flow was monitored by flow- and pressure sensors. The numerical study was conducted by solving the steady RANS equations and a $k - \varepsilon$ turbulence model. They discovered that the discharge coefficient of the two staged orifices was greater than that of the single staged orifice with the same diameter. They also discovered that under the same flow rate, the pressure drop of the two staged orifices was less than that of the single staged orifice, and it was concluded that the two staged orifices can improve the stability of the flow field at the outlet of the orifice.

In the previous studies, the effects of different β have not been extensively studied. In this study, the effects of different β and thicknesses of the orifice have been investigated for incompressible, viscous and laminar flow. The orifice Reynolds number range under investigation is $0 \leq Re \leq 100$, the orifice thickness to pipe diameter ratio varies between $1/8 \leq t \leq 2$ and the orifice diameter to pipe diameter ratio varies between $1/4 \leq \beta \leq 3/4$. The paper is organized as follow: Firstly, a grid resolution study with four different grid resolutions is presented for orifice with $\beta = 0.25$, $t=0.25$ at $Re = 100$. Secondly, results of the discharge coefficient for orifice with $\beta = 0.5$, orifice thickness $t = 0.125, 0.25, 0.5$ and 1 are presented and validated against previous numerical and experimental results. Thirdly the effects of different orifice characteristics on the flow field are discussed. Finally, main conclusions are given.

2. Computational domain

2.1 Flow model

In the present study, the flow is assumed to be laminar, incompressible and viscous. The governing equations are continuity equation and momentum conservation equations, given by:

$$\frac{\partial u_i}{\partial x_i} = 0 \tag{1}$$

$$\frac{\partial u_i}{\partial t} + u_j \frac{\partial u_i}{\partial x_j} = -\frac{1}{\rho}\frac{\partial p}{\partial x_i} + \nu \frac{\partial^2 u_i}{\partial x_j \partial x_j} \tag{2}$$

where $i, j = 1,2,3$. x_1, x_2, x_3 denote the streamwise and the two-cross-stream directions (also denoted as x in the following), respectively and u_1, u_2, u_3 are the corresponding velocity components. p is the pressure and ρ is the density of the fluid.

2.2 Numerical simulation schemes, computational domain and boundary conditions

The open source computational fluid dynamics (CFD) code OpenFOAM is employed to carry out the simulations. A merged PISO-SIMPLE solver pimpleFoam is used in the present study. The spatial schemes for gradient, divergence and Laplacian are Gauss linear, bounded Gauss upwind and Gauss linear corrected, respectively and all these schemes are in second order. The second Euler scheme is used for the time integration.

The computational domain consists of a circular, square edged orifice inserted at $L/2$ inside a pipe with a diameter of $D = 1$m as shown in Fig. 1. The pipe length is set to be $L = 10D$ without the additional length from the orifice thickness. Seven different cases are simulated at different Reynolds numbers (defined based on the average inlet velocity and the diameter of the pipe), where the orifice thickness to pipe diameter ratios are $t = 0.125, 0.25, 0.5, 1, 2$ and the orifice height to pipe diameter are $\beta = 0.25, 0.5, 0.75$. The Reynolds number in this study are $Re = 4, 16, 36, 64, 81, 100, 400$.

The boundary conditions are set as following:

At the inlet, a parabolic laminar velocity profile $u_1 = u_{max}[(1-r/R)^2]$ (where u_{max} is the centerline velocity, r is the distance to the pipe center and R is the radius of the pipe), $u_2 = 0, u_3 = 0$ is prescribed, and the pressure is set to be zero normal gradient.

At the outlet, the velocity is set as zero normal gradient and the pressure is set to be zero.

On the walls of the orifice plates and the pipe, no slip boundary condition is used for the velocities $u_1 = u_2 = u_3 = 0$ and the pressure is set as zero normal gradient.
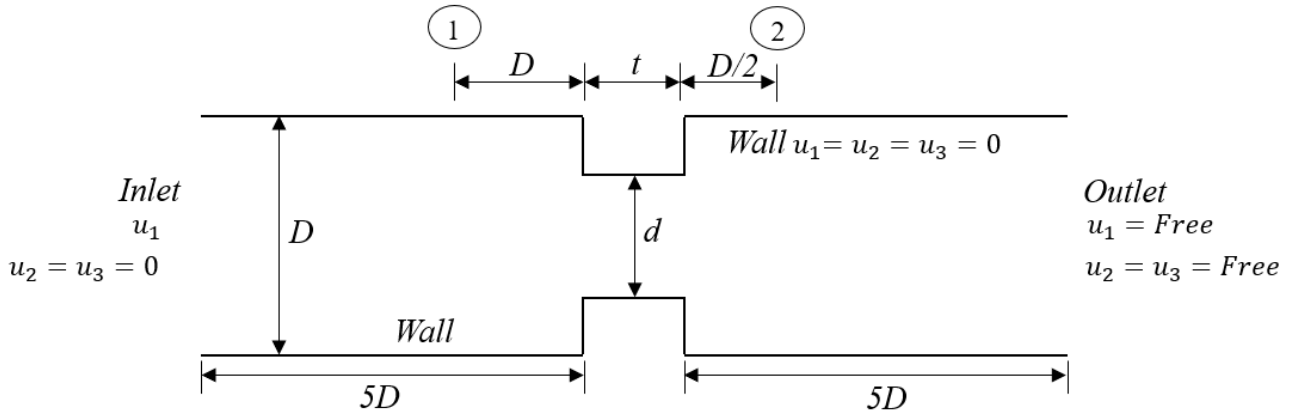

Fig. 1 Computational domain and boundary conditions
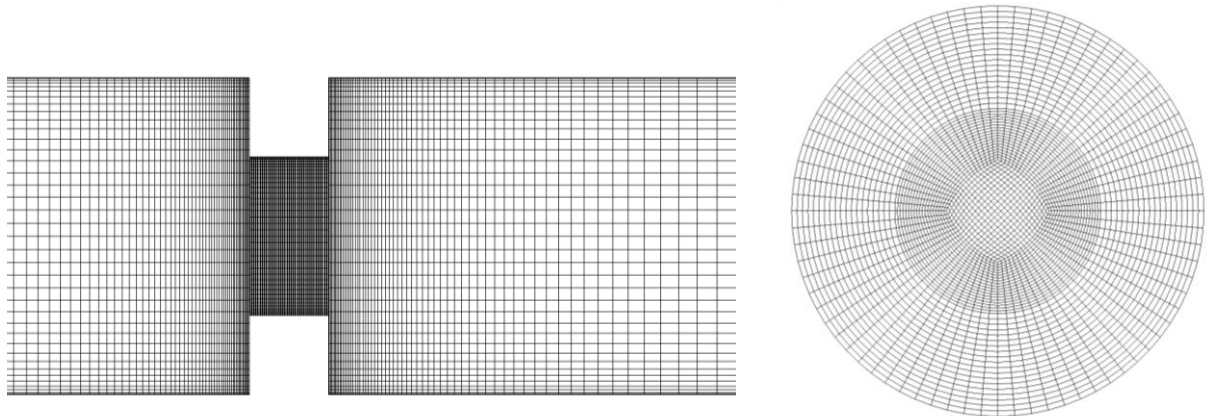
Fig. 2 Example of Mesh 2, $\beta = 0.5$ and t=0.5, around orifice region and grid inside pipe

2.3 Grid resolution and validation study

The computational grids in the axis and cross section directions of the present study are shown in Fig. 2. The grids in the axis direction are refined near the orifice plate. To ensure that the simulation results are fully converged inside the pipe, a grid convergence study is carried out. Four grid resolutions from coarse to fine are selected. Fig. 3 shows the pressure distributions $p^* = p/\rho$ along the pipe axis for different grid resolutions and Table 1 presents the relative differences in the pressure through the orifice with the finest grid of Mesh 4.

Table 1. Results of the cases with different grid resolution
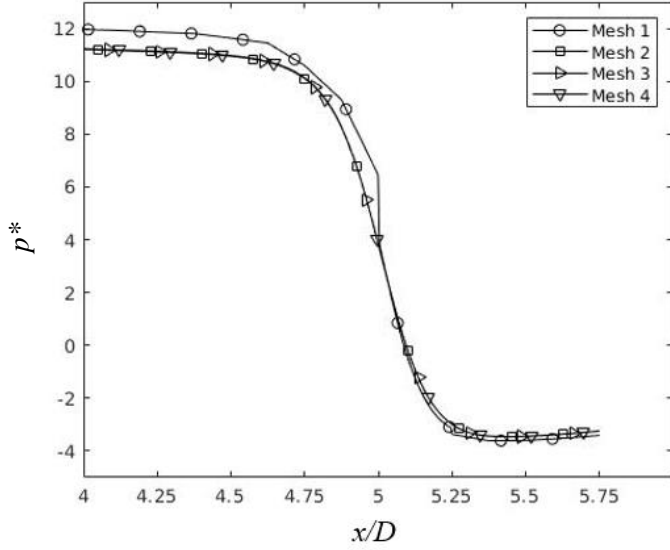
Case	Elements	Mean deviance from Mesh 4
Mesh 1	404 320	20.949%
Mesh 2	968 968	0.344%
Mesh 3	2 303 120	0.092%
Mesh 4	3 040 552	-

Fig. 3 Pressure distributions p*=p/ρ for four different grid resolutions

It is shown that there is negligible difference in the pressures among Mesh 2,3,4 and Mesh 2 is sufficient to produce fully converged results. Taking the computational amount into consideration, the grid resolution of Mesh 2 is chosen for the whole simulation in the present study.

Validation of the results is carried out by comparing the discharge coefficient (3) obtained from the numerical results for different orifice thickness at different Reynolds numbers with previous numerical and experimental data obtained by Sahin & Ceyhan (1996).

$$C_d = \frac{1}{2\sqrt{2}}\left(\frac{1}{\beta}\right)^2(1-\beta^4)^{1/2}\frac{1}{\sqrt{\Delta P}} \tag{3}$$

The discharge coefficient is a function of orifice diameter to pipe diameter ratio β, and pressure loss through the orifice $\Delta p = p_1^* - p_2^*$, where p_1^* is the pressure measured at probe location 1 and p_2^* is the pressure measured at probe location 2 as shown in Fig. 1. The parameters and the grids numbers for validation are shown in Table 2. The results of the present study are compared with the published data in Fig. 4. In general, the present results are in good agreement with the experimental and numerical data of Sahin & Ceyhan (1996). For large t at high Reynolds numbers, the present results are in good agreement with the data of Sahin & Ceyhan (1996). For small t in Fig. 4 (a), (b), the present results are slightly higher than the experimental and numerical data of Sahin & Ceyhan (1996). There are underestimations at $Re = 16$ for $t = 0.125$ and at $Re = 4$ for $t = 0.25$. Further comparisons are made for different t at Re =100 in Table 3. It can be seen that for smaller t, there is approximately 4.35% difference in the present results from the those of the previous numerical simulations and 6% from the experimental results.

Table 2 Cases in validation study

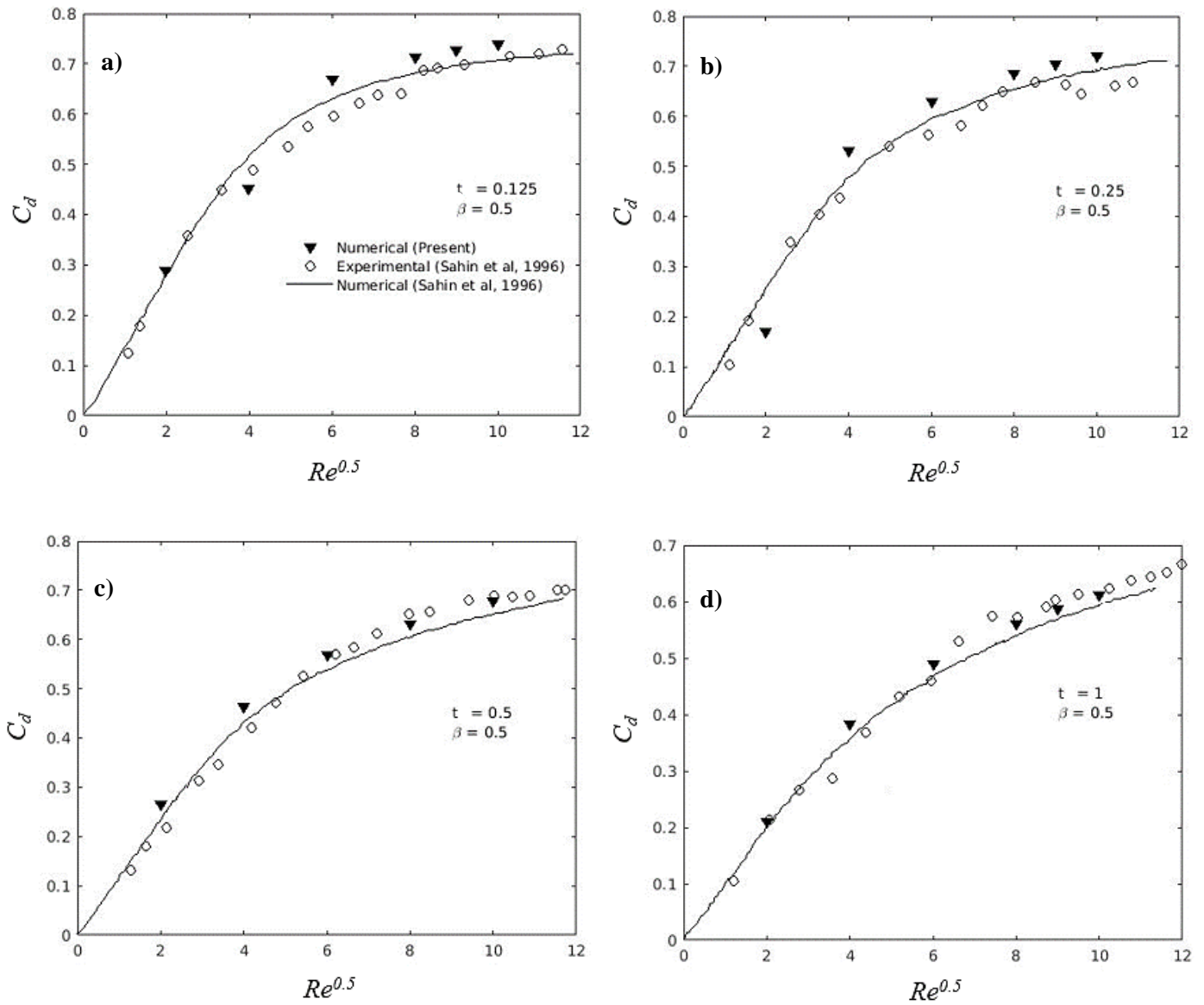| Case	β	t	Cells
1	0.5	0.125	1 128 560
2	0.5	0.25	993 282
3	0.5	0.5	968 968
4	0.5	1	1 011 520

Fig. 4 Variation of discharge coefficients with increasing Reynolds number, compared with results from Sahin & Ceyhan (1996)

Table 3 Validation of present numerical results compared with numerical and experimental results by Sahin & Ceyhan (1996)

No.	Author	Re	t	Numerical C_d	Experimental C_d
1	Present	100	0.125	0.7374	
2		100	0.25	0.7207	
3		100	0.5	0.6765	
4		100	1	0.6115	
5	Sahin & Ceyhan (1996)	100	0.125	0.7061	0.7155
6		100	0.25	0.6887	0.6614
7		100	0.5	0.6506	0.6900
8		100	1	0.5950	0.6223

3 Results and discussion

3.1 Discharge coefficients

Effects of different orifice characteristics on the discharge coefficient are discussed. The discharge coefficients of the present numerical simulations with variation of Reynolds number are shown in Fig. 5, ant the values are listed in Table 4. It can be observed for Case 5 the discharge coefficient increases aggressively from $0 \leq Re \leq 100$, and starts to be stable at $Re \geq 100$. It is worth mentioned that due to the small orifice diameter in Case 5, the acceleration of the flow after passing the orifice may cause weak turbulent flow. For Case 6 and Case 7, it can be observed that the discharge coefficient increases less rapidly than that of Case 5 at $0 \leq Re \leq 100$, and is still increasing from $Re = 400$. The larger β causes less restriction to the flow passing through the orifice, and the pressure drop is not so significant as that in Case 5.

Table 4 Overview of the different cases

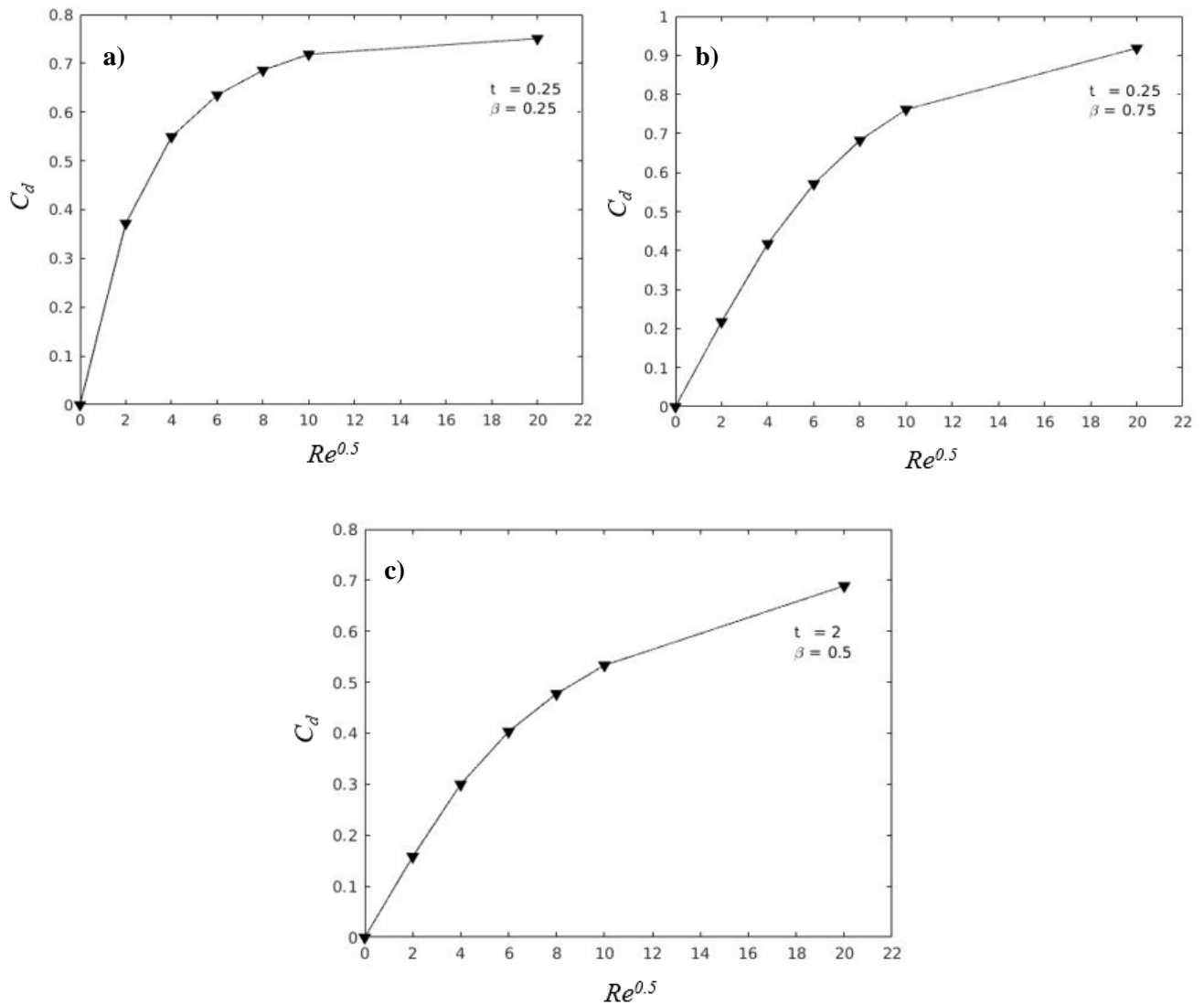| Case	β	t	Cells
5	0.25	0.25	1 128 560
6	0.75	0.25	993 282
7	0.5	2	1 282 080

Fig. 5 Variation of discharge coefficients with increasing Reynolds numbers for a) Case 5, b) Case 6, c) Case 7

Table 5 Discharge coefficients at different Reynolds numbers for different orifice characteristics

Case	β	t	C_d	C_d	C_d	C_d	C_d	C_d
			Re=4	*Re=16*	*Re=36*	*Re=64*	*Re=100*	*Re=400*
5	0.25	0.25	0.3718	0.5493	0.6350	0.6857	0.7185	0.7508
6	0.75	0.25	0.2174	0.4175	0.5708	0.6823	0.7615	0.9184
7	0.5	2	0.1581	0.2997	0.4033	0.4774	0.5333	0.7652

3.2 Flow pattern

3.2.1 Effect of Re on flow characteristics

Streamwise velocity contours, streamlines and Q criterion contours of Case 5 at *Re*= 16, 64, 100 are presented in Fig. 6. From the streamwise velocity contours, it can be seen that the flow is accelerated from a distance before the orifice plate and this is more prominent with increasing Reynolds numbers. Compression of the flow can be observed when the flow enters the orifice, and after the orifice, the flow appears to be a jet. The jet flow expansion is observed to shrink at higher Reynolds numbers, and the length of the jet is increased.

The streamlines in front of the orifice keep attached to the orifice because of the low Reynolds number, and are compressed when entering the orifice. In the outlet of the orifice, separation of the streamlines occurs, and the flow quickly re-attach to the pipe wall at the lower Reynolds numbers. The recirculation length becomes larger at higher Reynolds numbers.

The Q criterion is used to identify the vortical structures (Hunt et al. 1988), which is defined as

$$Q = \frac{1}{2}[|\Omega|^2 - |S|^2] > 0 \tag{4}$$

Where $\Omega = \frac{1}{2}\left(\frac{\partial u_i}{\partial x_j} - \frac{\partial u_j}{\partial x_i}\right)$ is the rotation tensor and $S = \frac{1}{2}\left(\frac{\partial u_i}{\partial x_j} + \frac{\partial u_j}{\partial x_i}\right)$ is the strain tensor.

It can be observed that vortical structures form both inside and after the orifice. The vortical structures inside the orifice tend to be tilted in the streamwise direction, and the vortical structure after the orifice tends to locate in the fringe of the recirculation motions. The strength of the vortical structures reduces with increasing Reynolds number, which is due to the increasing rate of strain in the flow with increasing Reynolds number.
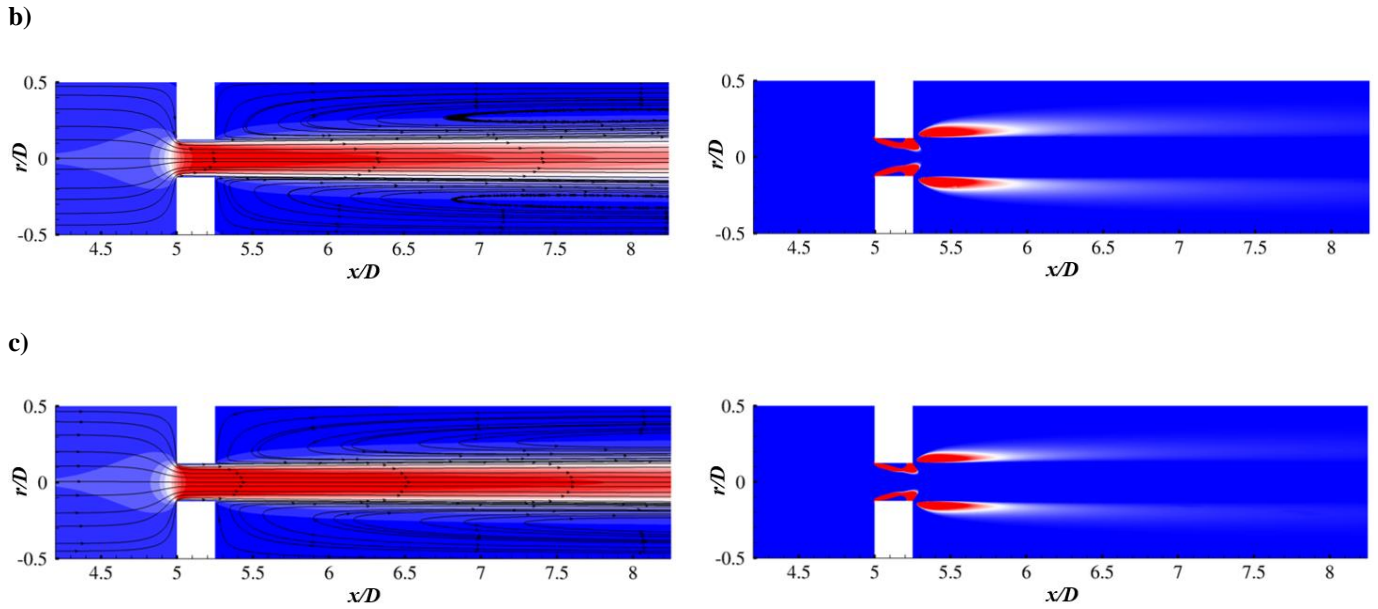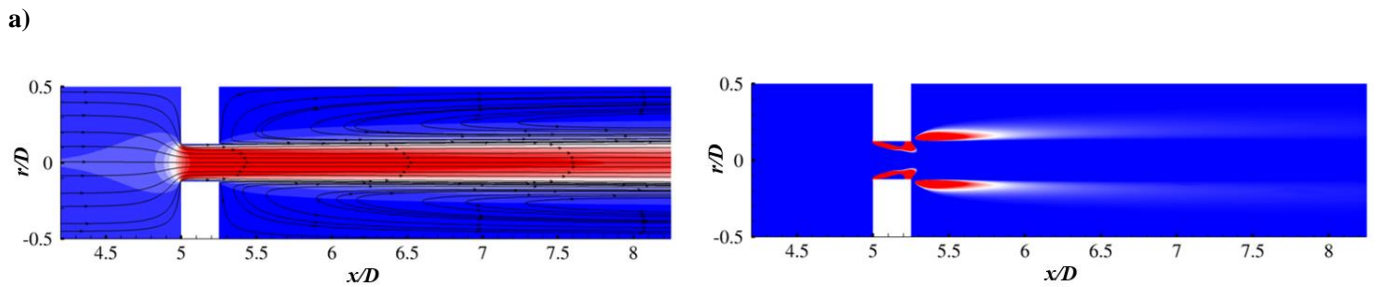
a)

b)

c)
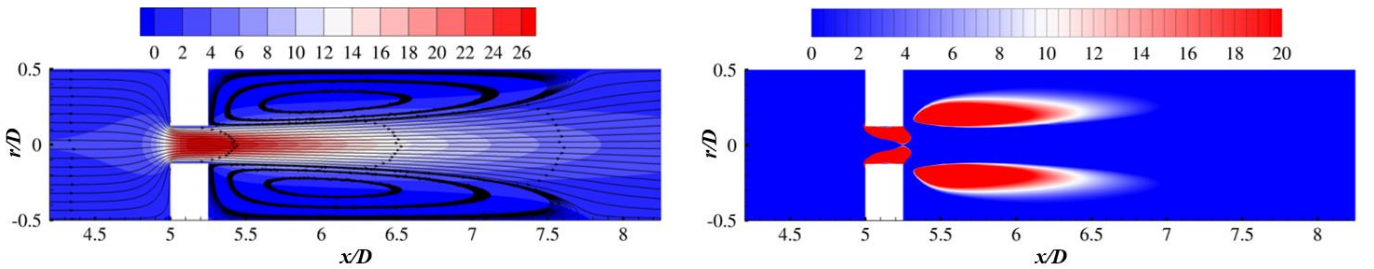
Fig. 6 Streamwise velocity contours, streamlines and Q criterion contours for Case 5, (a) *Re* =16, (b) *Re* = 64 and (c) *Re* = 100.

3.2.2 Effect of β on flow characteristics

Table 6 shows the recirculation length with varying β at Re = 16 as an example. Flow separation occurs from the inlet of the orifice plate due to the adverse pressure gradient, and the recirculation length is the distance between the point of separation and the point of the flow re-attachment. The recirculation length decreases with increasing β. Further comparisons are made for streamwise velocity contours, streamlines as well as Q criterion contours at Re = 100. From the streamwise velocity contours, the acceleration region in front of the orifice is expanded and the recirculation length is shortened with increasing β. In the Q contours, it is shown that with higher β, the strength of the vortical structures reduces and almost disappears with $\beta = 0.75$. From $\beta = 0.25 \sim 0.5$ in Fig 7 (a)~(b), it can be seen that the vortical structures strengthen in the orifice. In Fig. 7 (c), the vortical structures tend to be separated into two small eddies, which are located in the two edges of the orifice plates.

Table 6 Length of separated flow with respect to change in β at Re=16

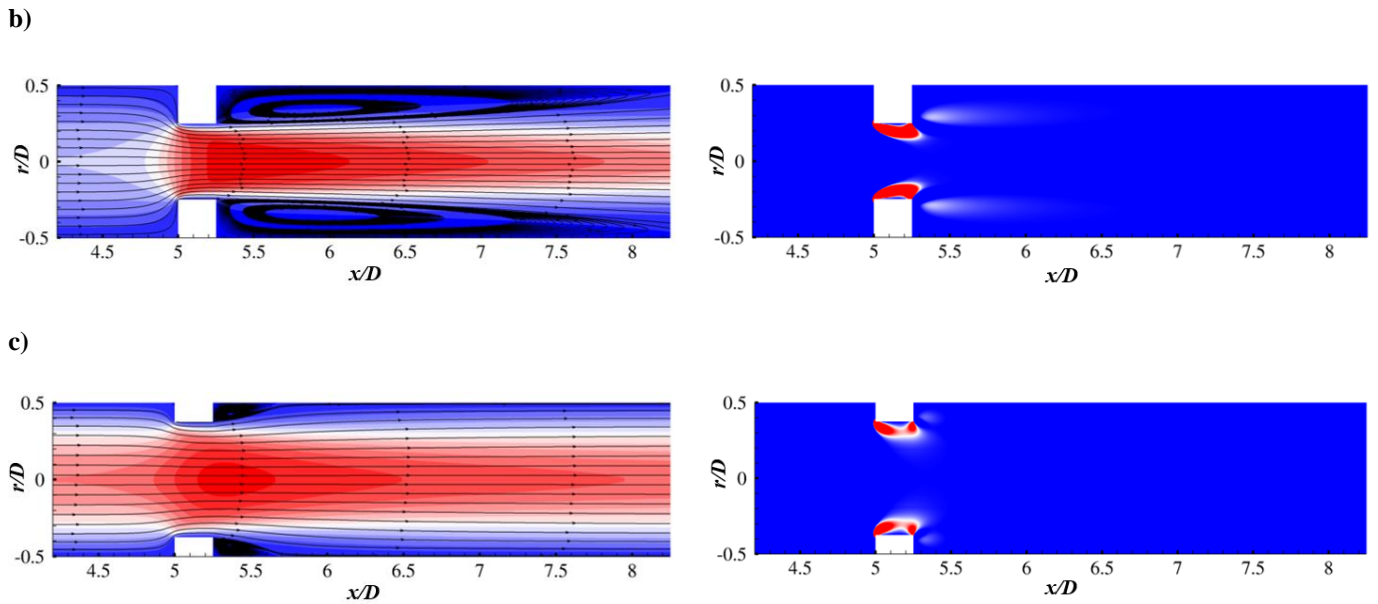| β	Recirculation length (*l/D*)
0.25	2.5391
0.5	0.6766
0.75	0.1410

a)

b)

c)

Fig. 7 Streamwise velocity contours, streamlines and Q criterion contours at Re = 100 for (a) Case 5, (b) Case 2 and (c) Case 6.

3.2.3 Effect of t on flow characteristics

In Fig.8, the dependencies of streamwise velocity contours, streamlines and Q criterion contours on t are shown. It can be observed that there is negligible change in the streamwise velocity contours with varying t. It can also be seen that increasing the thickness does not seem to alter the recirculation length significantly, which is also observed in the results in Sahin & Ceyhan (1996). The vortical structures after the orifice becomes slightly weaker with larger t . When $t = 0.125$ and $t = 0.25$, there is only one vortical structure formed inside the orifice. With t =0.5, the vortical structure starts separating and with t =1, 2 the vortical structure is formed into two regions in the upstream and downstream, located at the inlet and edge of the orifice and the two vortical structures are weakly interacted.
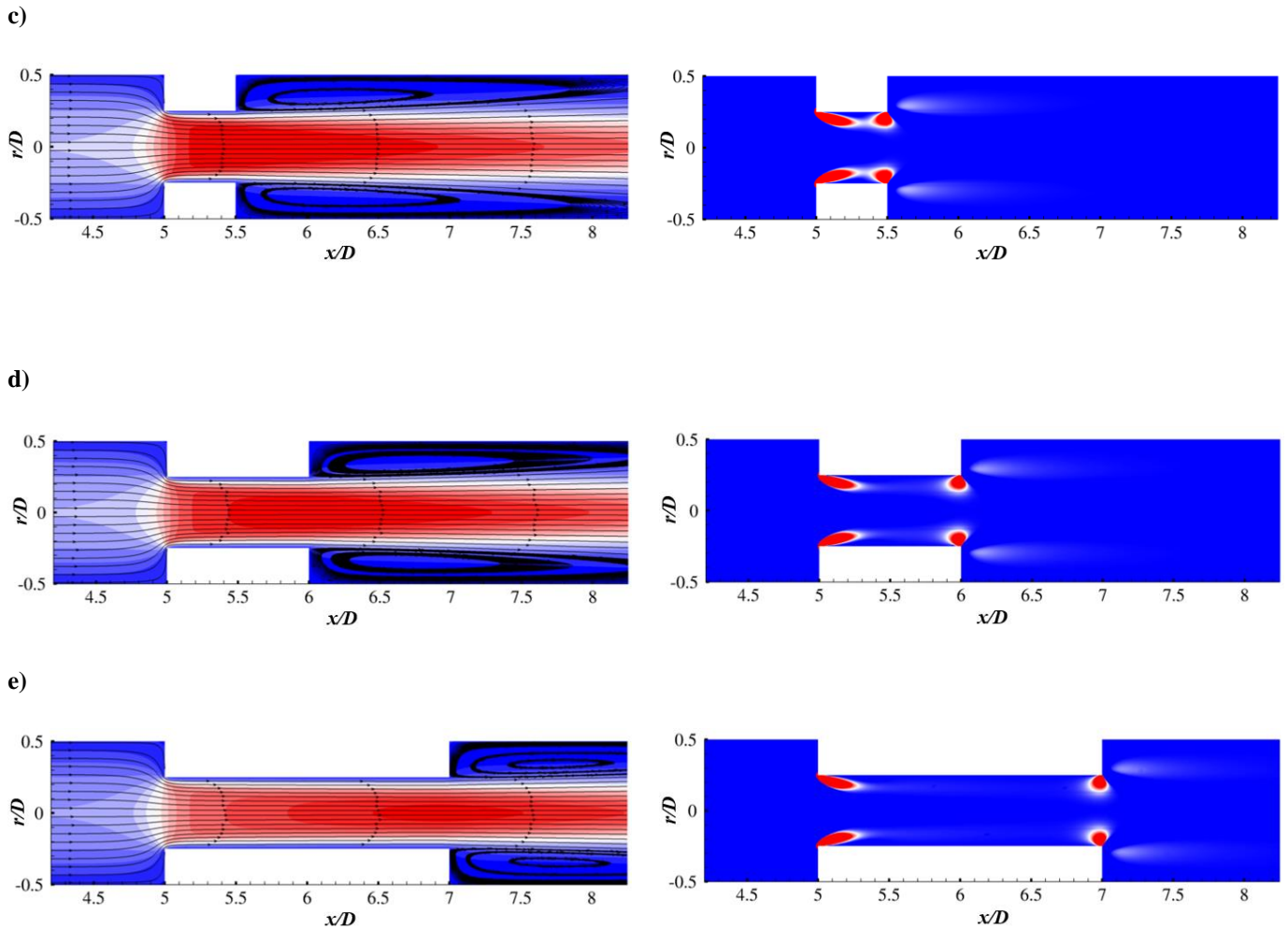
a)

b)

c)

d)

e)
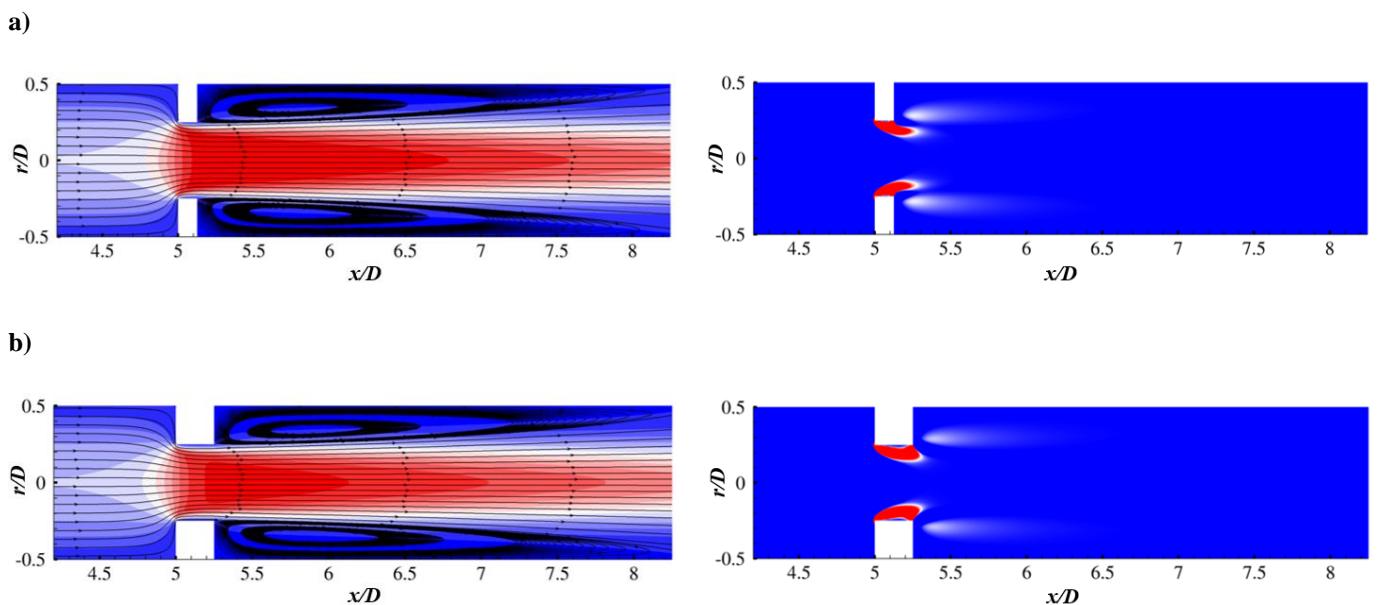
Fig. 8 Streamwise velocity, streamlines and Q criterion contours at Re = 100 for (a) Case 1, (b) Case 2, (c) Case 3, (d) Case 4 and (e) Case 5.

4. Conclusion

Numerical investigations for orifice flowmeters have been carried out and validated against previous experimental and numerical results. Grid convergence study has been performed to ensure sufficient grid resolution of the present results and also keep the computational cost low. Flow through seven orifice flowmeters with different orifice heights and thicknesses ratios has been simulated. The resulting discharge coefficients and flow fields for different parameters are presented. The main conclusions are as follows:

1) The resulting discharge coefficients are in good agreement with the published numerical and experimental data, except that there are underestimations at low Reynolds number.

2) The vortical structure after the orifice is weakened with increasing Re and β. The vortical structure in the orifice separates with increasing t* and two vortical structures forms at the two edges of the orifice plates.

3) The recirculation length of the flow increases with increasing Reynolds number and decreases with increasing β and there is no significant change with increasing t*. The flow re-attaches to the pipe wall quickly at low Reynolds number for large β. However, at higher Reynolds number at smaller β the recirculation length cannot be predicted as the re-attachment occurs outside the computational domain.

References

Dickerson P. & Rice W. 1969. An investigation of very small diameter laminar flow orifices, Transactions of the ASME, 546-548.

Gao J. & Wu F. 2019. Investigation of flow through the two-stage orifice, Engineering Applications of Computational Fluid Mechanics, 13:1, 117-127, DOI: 10.1080/19942060.2018.1561517.

Hollingshead C.L., Johnson M.C., Barfuss S.L. & Spall R.E. 2011. Discharge coefficient performance of Venturi, standard concentric orifice plate, V-cone and wedge flow meters at low Reynolds numbers, Journal of Petroleum Science and Engineering 559-566.

Holzmann T. 2017. Mathematics, Numerics, Derivation and openFOAM. Holzmann CFD, Leoben, fourth edition, pp 37-39.

Hornbeck R.W. 1964. Laminar flow in the entrance region of a pipe. Appl. sci. Res 13: 224. https://doi.org/10.1007/BF00382049.

Hunt J. C. R., Wray A. & Moin, P. 1988. Eddies, stream, and convergence zones in turbulent flows. Center for Turbulence Research Report CTR-S88.

Lakshmana Rao N.S. & Sridharan K. 1971. Loss characteristics of long orifices, Fourth Australian conference on hydraulics and fluid mechanics, 246-251.

Miller R. W. 1997. Flow Measurement Engineering Handbook, 3rd ed. New York: McGraw-Hill.

Mittal R.C. & Sharma P.K. 1987. Numerical solution of a viscous incompressible flow problem through an orifice, Applied Scientific Research 44 361-375.

Sahin B. & Ceyhan H. 1996. Numerical and experimental analysis of laminar flow through square-edged Orifice with variable thickness, Transactions of the Institute of Measurement and Control, Vol 18(4), 166-174.

Tunay T., Sahin B. & Akilli H. 2004. Investigation of Laminar and Turbulent flow through an orifice plate inserted in a pipe, Transactions of the CSME/de la SCGM, Vol 28. No.2B 403-414.